Supplementary Materials for

Prediction of Perovskite Oxygen Vacancies for Oxygen Electrocatalysis at Different Temperatures

Zhiheng Li[1,2,8£], Xin Mao[3£], Desheng Feng[1£], Mengran Li[4]*, Xiaoyong Xu[1,5]*, Yadan Luo[6]*, Linzhou Zhuang[7], Rijia Lin[1], Tianjiu Zhu[1], Fengli Liang[1], Zi Huang[6], Dong Liu[8], Zifeng Yan[8], Aijun Du[3], Zongping Shao[9]* and Zhonghua Zhu[1]*

Affiliations:

1. School of Chemical Engineering, The University of Queensland, Brisbane, 4072, Australia
2. Center of Artificial Photosynthesis for Solar Fuels and Department of Chemistry, School of Science and Research Center for Industries of the Future, Westlake University, Hangzhou 310030, China.
3. School of Chemistry and Physics and Centre for Materials Science, Queensland University of Technology, Brisbane, 4001, Australia
4. Department of Chemical Engineering, The University of Melbourne, Melbourne, 3010, Australia
5. School of Chemical Engineering, The University of Adelaide, Adelaide, 5005, Australia
6. School of Information Technology and Electrical Engineering, The University of Queensland, Brisbane, 4072, Australia
7. School of Chemical Engineering, East China University of Science and Technology, Shanghai, 200237, China
8. School of Chemical Engineering, China University of Petroleum, Qingdao, 266580, China
9. WASM: Minerals, Energy and Chemical Engineering, Curtin University, Perth, 6102, Australia

*Correspondence to:

M. Li: aaron.li1@unimelb.edu.au

X. Xu: xiaoyong.xu@adelaide.edu.au

Y. Luo: y.luo@uq.edu.au

Z. Shao: zongping.shao@curtin.edu.au

Z. Zhu: z.zhu@uq.edu.au

£ Z. Li, X. Mao, and D. Feng make equal contributions to this paper.

1. Supplementary figures

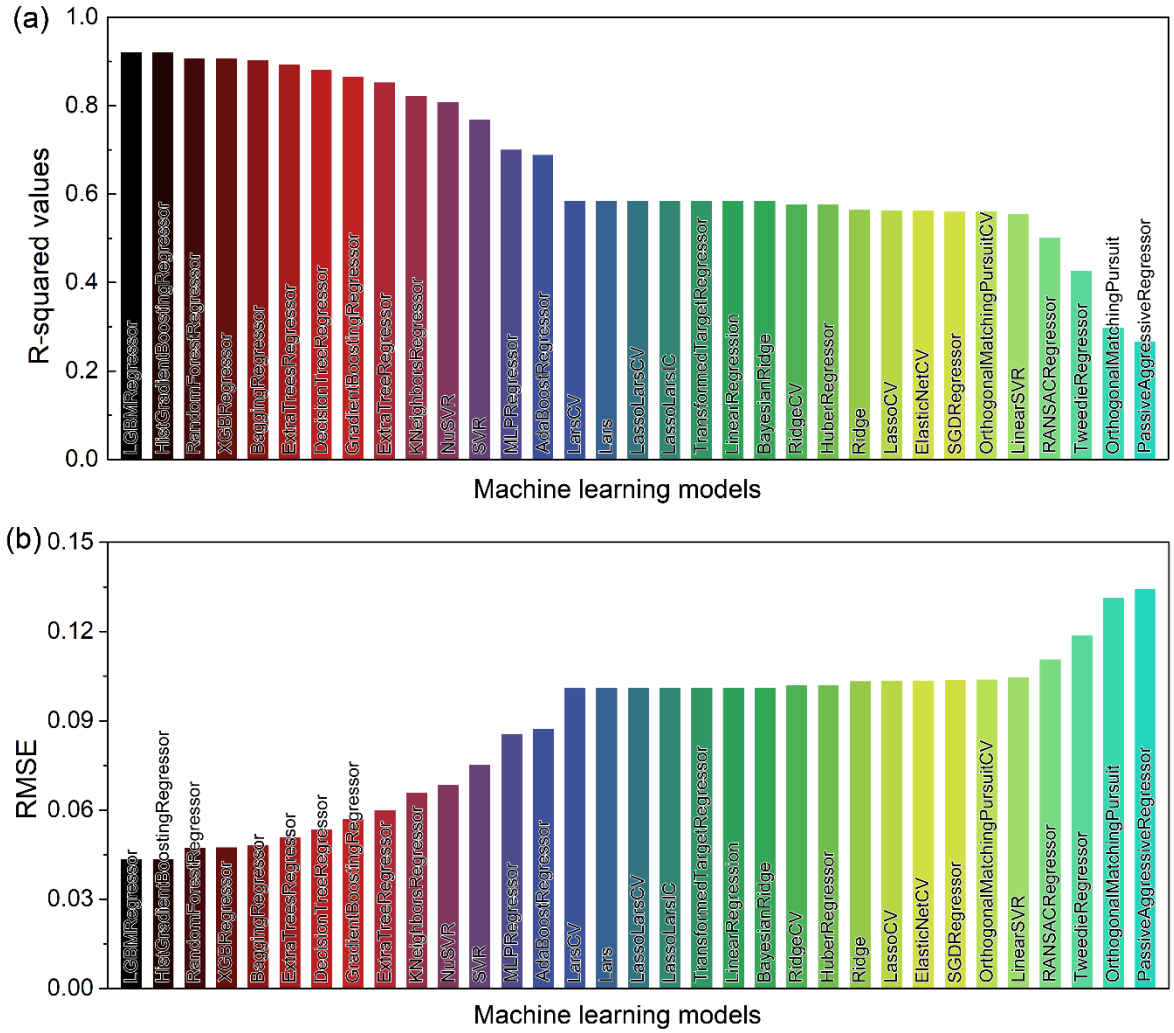

Supplementary Fig. S1 (a) R-squared and **(b)** RMSE values of top 33 machine learning models. The R-squared and RMSE scores are the averaged mean of the 5 random tests (5-fold cross-validation).

Supplementary Note 1:

Seven properties of cations in $ABO_{3-\delta}$ perovskites, including electronegativity (χ), polarization power (P), charge (Z), cation A-size (r_A), cation B-size (r_B), tolerance (τ), and temperature (T) were used for the machine learning models. To better reflect the inductive effect of the cations at A-sites and dopants at B-sites (i.e., non-active cations) towards active metal centers (e.g., Co and Fe), these properties were calculated by weighing the stoichiometries of non-active cations according to the following equations:

$$\chi = sum(S_i \cdot \chi_i) / sum(S_i) \quad \textbf{Eq. S1}$$

$$P = sum(S_i \cdot r_i^{1/2} / Z_i) / sum(S_i) \quad \textbf{Eq. S2}$$

$$Z = sum(S_i \cdot Z_i) / sum(S_i) \quad \textbf{Eq. S3}$$

$$r_A = sum(S_{Ai} \cdot r_{Ai}) / sum(S_{Ai}) \quad \textbf{Eq. S4}$$

$$r_B = sum(S_{Bi} \cdot r_{Ai}) / sum(S_{Bi}) \quad \textbf{Eq. S5}$$

$$\tau = (r_A + r_O) / \left[\sqrt{2} \cdot (r_B + r_O)\right] \quad \textbf{Eq. S6}$$

where S_i is the stoichiometry of the non-active cation i, χ_i is the electronegativity of the non-active cation i, $r_i^{1/2} / Z_i$ is the polarization power of the non-active cation i, Z_i is the charge of non-active cation i, r_{Ai} and r_{Bi} are the ionic radii of the non-active cation i, respectively, and r_O is the ionic radii of oxygen.

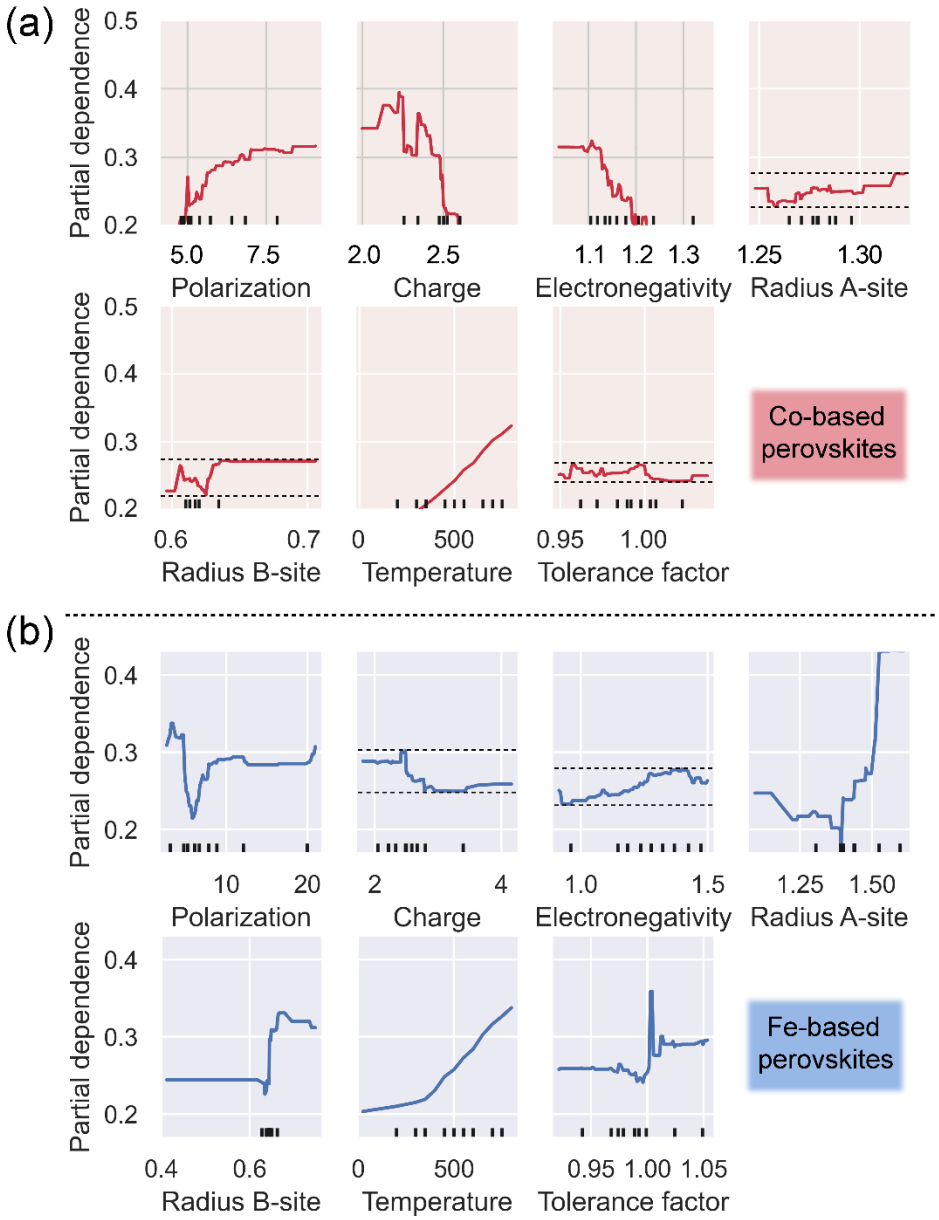

Supplementary Fig. S2 Partial dependence from LGBM Regressor machine learning model over polarization power, charge, electronegativity, radius A-site, radius B-site, temperature, and tolerance factor for (**a**) Co-based and (**b**) Fe-based perovskites. The dashed lines are guidance for showing the features with low dependence on machine learning model.

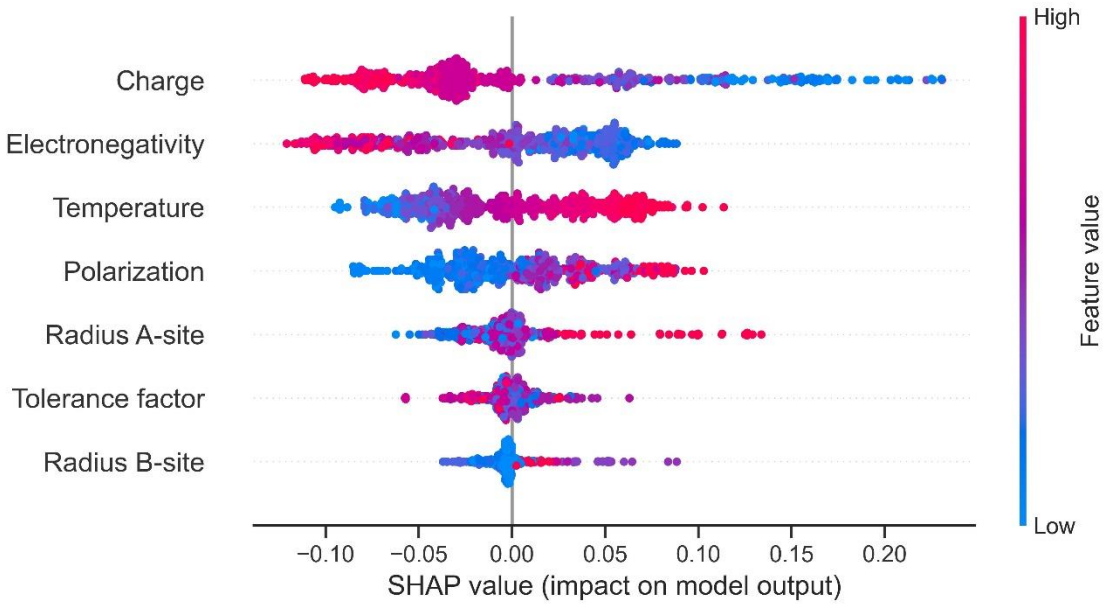

Supplementary Fig. S3 Distribution of all SHAP values for the seven features. The features are listed on the y-axis in descending order of their importance, based on the mean absolute SHAP value.

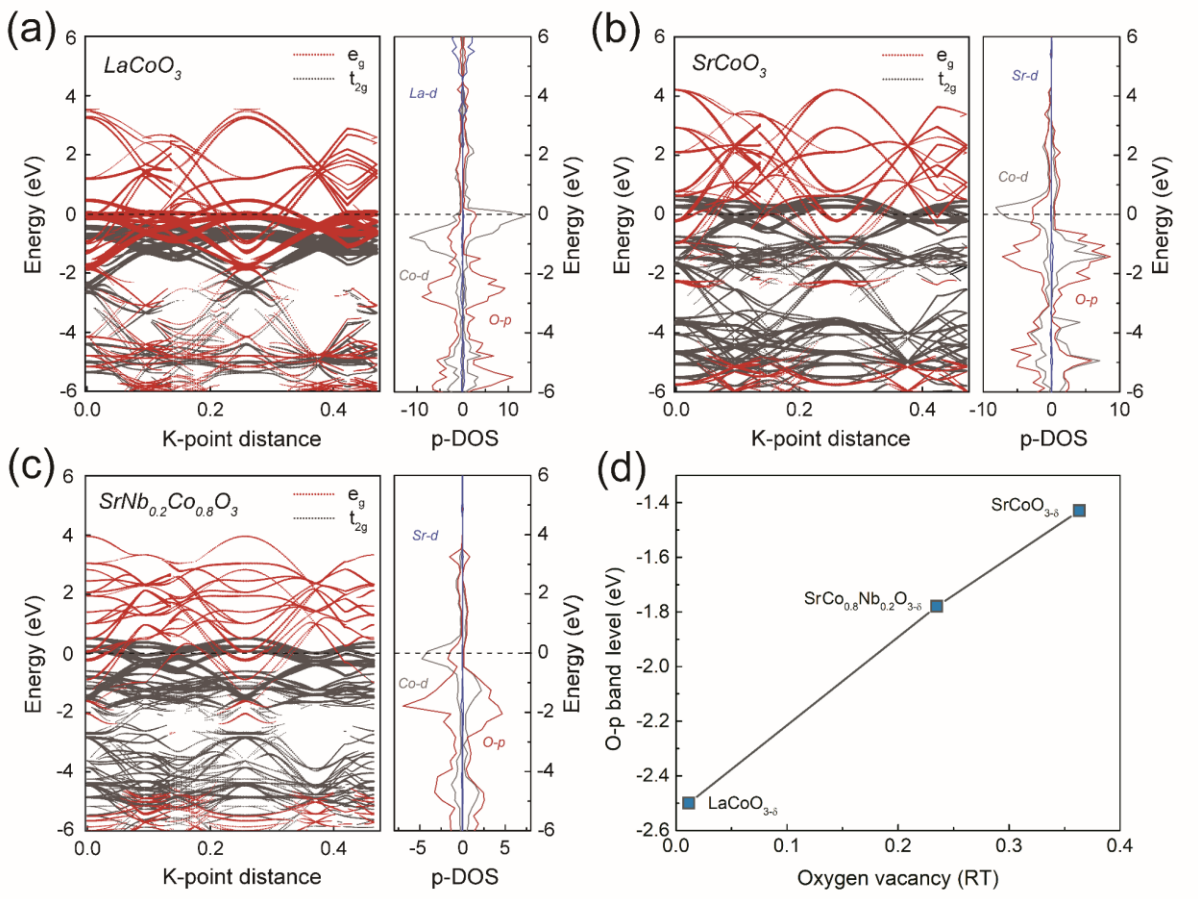

Supplementary Fig. S4 Band structures for representative oxides of (**a**) $LaCoO_3$, (**b**) $SrCoO_3$, and (**c**) $SrCo_{0.8}Nb_{0.2}O_3$ with the partial density of La-d, Co-d, and O-p states. (**d**) Relationship between O-p band level and oxygen vacancy for the three oxides.

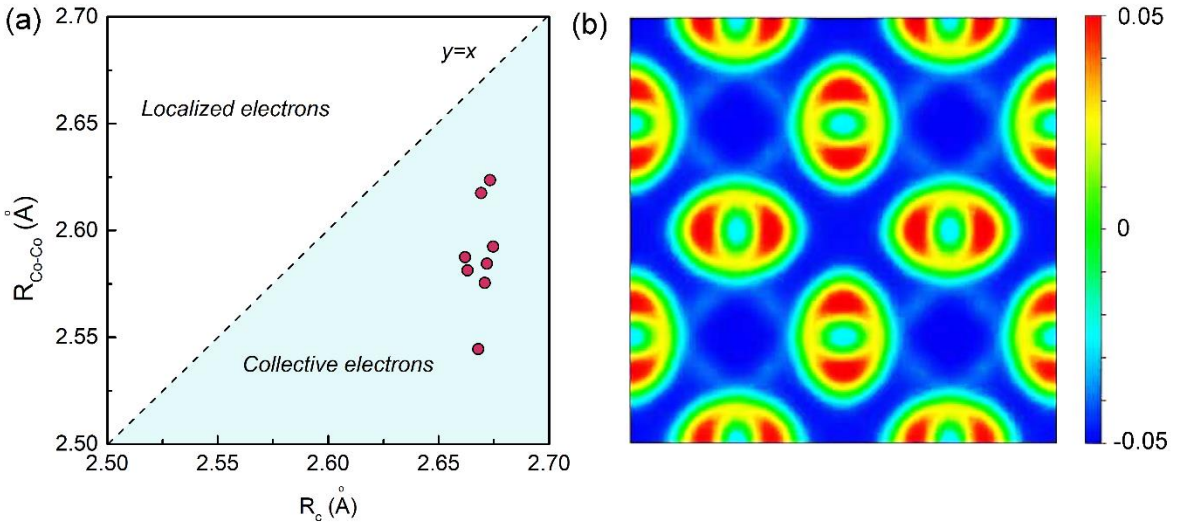

Supplementary Fig. S5 Electronic state measurements for perovskite oxides. (**a**) Comparison of R_{Co-Co} with R_c for Co-based perovskites (e.g., $SrCo_{0.8}V_{0.2}O_{3-\delta}$, $SrCo_{0.8}Nb_{0.2}O_{3-\delta}$, $SrCo_{0.8}Ta_{0.2}O_{3-\delta}$, $SrCo_{0.8}Nb_{0.1}Ta_{0.1}O_{3-\delta}$, $Ba_{0.5}Sr_{0.5}Co_{0.8}Fe_{0.2}O_{3-\delta}$, $SrSc_{0.175}Nb_{0.025}Co_{0.8}O_{3-\delta}$, $SrCo_{0.8}Ta_{0.1}V_{0.1}O_{3-\delta}$and $SrCo_{0.8}Ta_{0.175}V_{0.025}O_{3-\delta}$. (**b**) Surface electrostatic potential for representative $SrCo_{0.8}Ta_{0.175}V_{0.025}O_{3-\delta}$ oxide.

Supplementary Note 2:

To determine the electronic properties in the 3d orbital of Co-based perovskites, efforts were made to calculate the critical radius (R_c) from [1]:

$$R_c(3d) = 3.2 - 0.05n - 0.03(Z - Z_{Ti}) - 0.04S(S+1) \quad \textbf{Eq. S7}$$

where n is the oxidation state of Co, Z and Z_{Ti} are atomic numbers of Co and Ti, respectively, and S represents the total spin quantum number of 3d electrons for Co.

Meanwhile, the R_{Co-Co} was statistically calculated from the lattice structure of Co-based perovskites, after being optimized by theoretical calculation. The Co radius could be obtained from a database established by Shannon [2], Pauling [3], and Matar [4]. The $R_c < R_{Co-Co}$ indicates that the electrons are collective. The DFT result also shows the collective character of the electrons over $SrCo_{0.8}Ta_{0.175}V_{0.025}O_{3-\delta}$ perovskite.

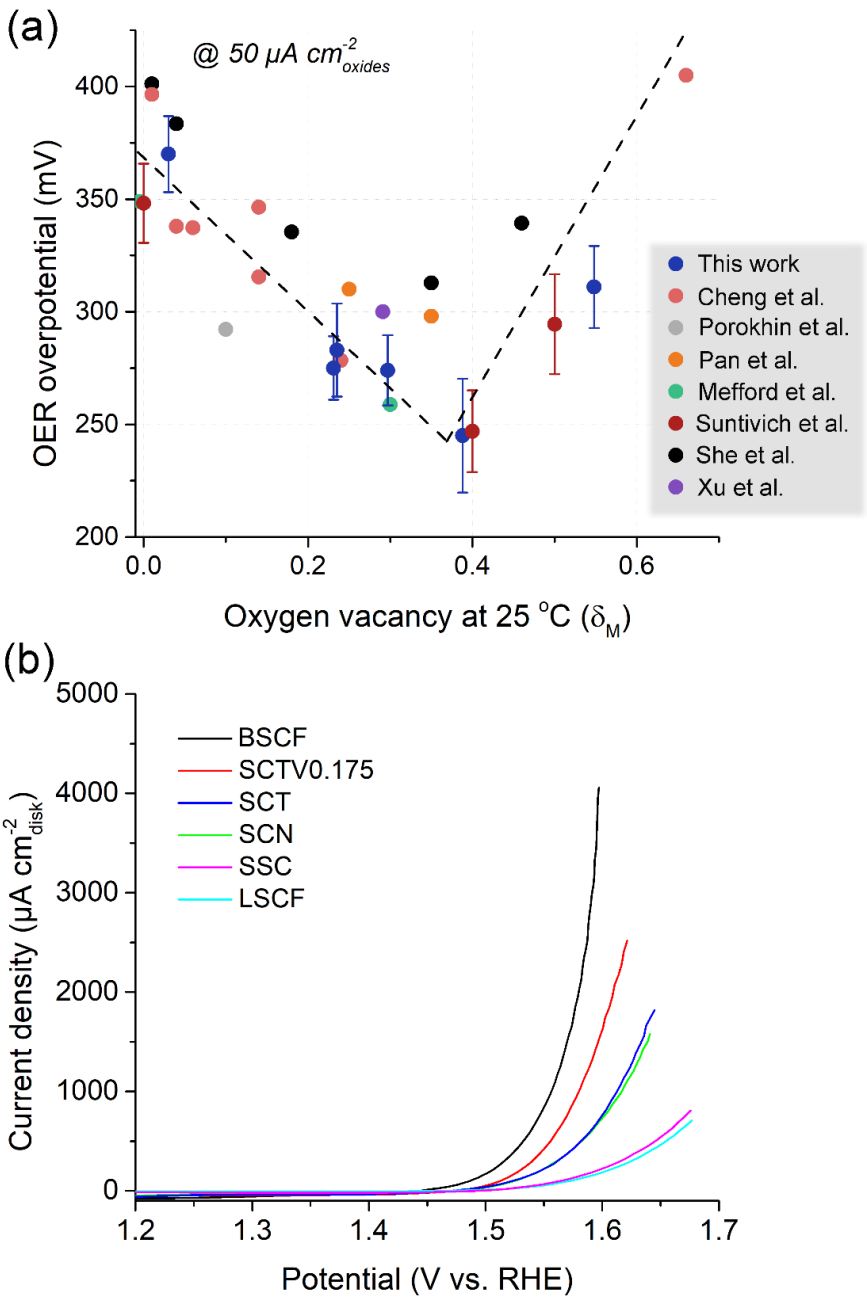

Supplementary Fig. S6 (a) Volcano relationship between OER overpotentials and oxygen vacancy for various perovskites. The data were collected from the references (Cheng et al.[5], Porokhin et al.[6], Pan et al.[7], Mefford et al.[8], Suntivich et al.[9], She et al.[10], and Xu et al.[11]) and tested by ourselves (blue ones, mean values ± S.D.) in 0.1 M KOH. The dashed lines are demonstrated for guidance. (b) OER polarization profiles of perovskite catalysts synthesized in this work. The measurements were conducted at a scan rate of 5 mV s^{-1} at room temperature with a RDE rotation rate of 3000 rpm. All measurements were repeated for three times.

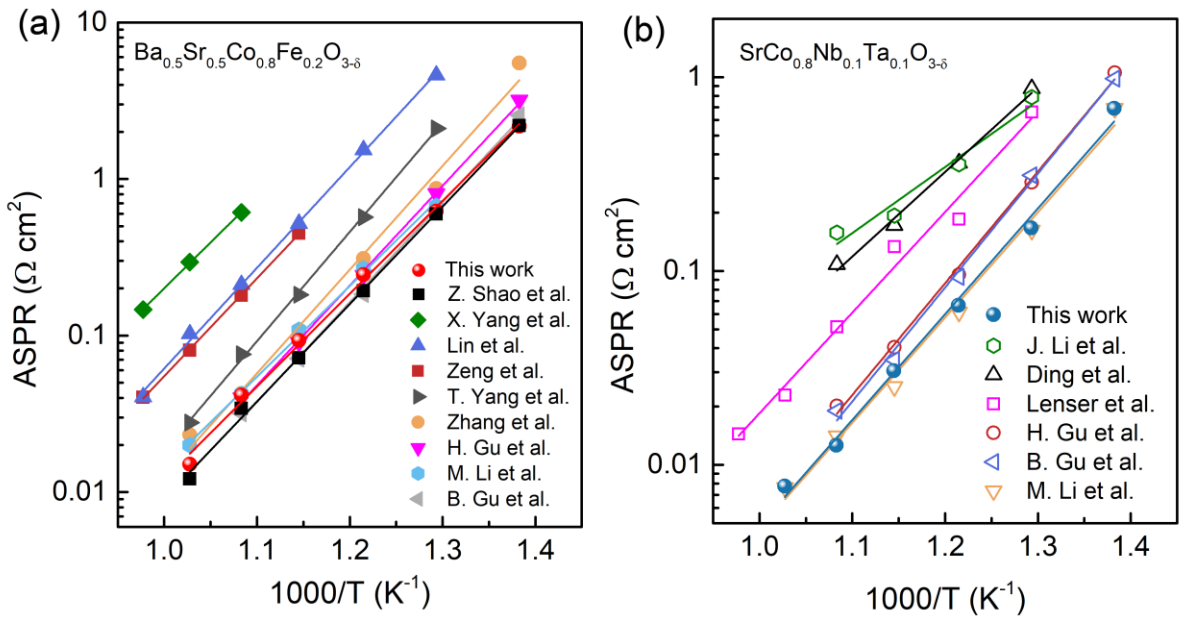

Supplementary Fig. S7 Difference in ORR performance (i.e., ASPR values) among reports of (a) $Ba_{0.5}Sr_{0.5}Co_{0.8}Fe_{0.2}O_{3-\delta}$ and (**b**) $SrCo_{0.8}Nb_{0.1}Ta_{0.1}O_{3-\delta}$ perovskites from different groups.

Supplementary Note 3:

The BSCF results are summarized from Z. Shao et al. [12], X. Yang et al. [13], Lin et al. [14], Zeng et al. [15], T. Yang et al. [16], Zhang et al. [17], H. Gu et al. [18], M. Li et al. [19], and B Gu et al [20]. The SCNT results are summarized from J. Li et al. [21], Ding et al. [22], Lenser et al. [23], H. Gu et al. [18], B. Gu et al. [20], and M. Li et al. [19]

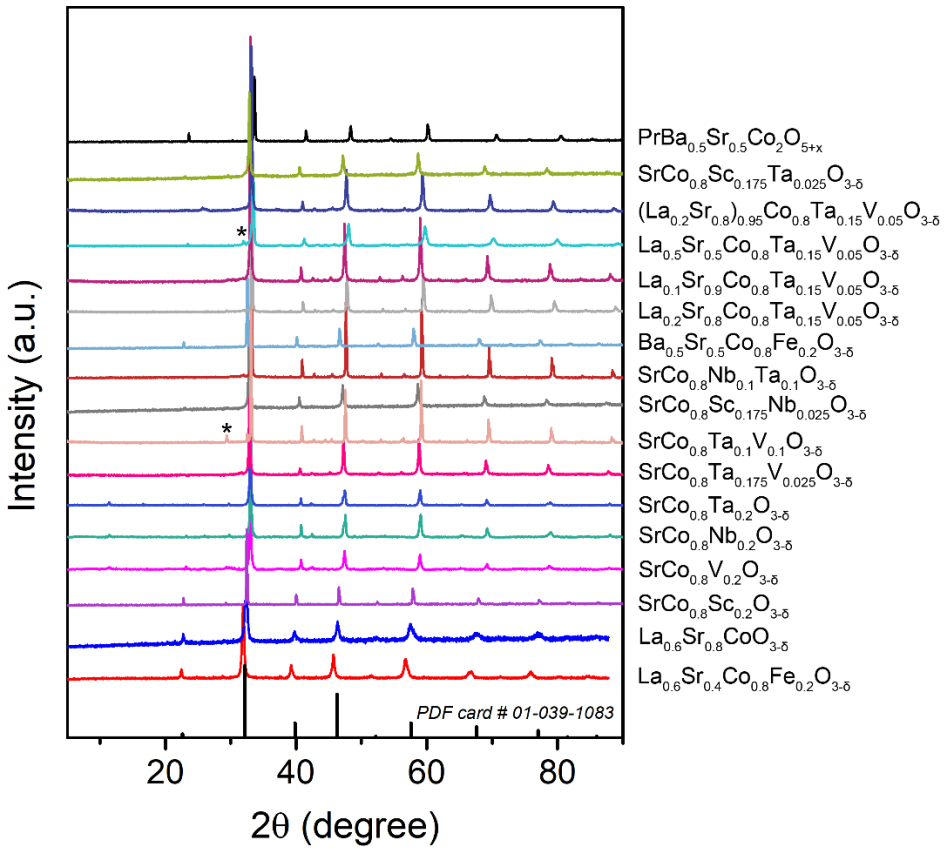

Supplementary Fig. S8 X-ray diffraction (XRD) spectrum of various perovskites synthesized by ourselves. The * symbols mean minor phase in perovskite structure. The XRD patterns of $Sr_{0.95}Ag_{0.05}Nb_{0.1}Co_{0.9}O_{3-\delta}$ (SANC) and $Ba_2Bi_{0.1}Sc_{0.2}Co_{1.7}O_{5+x}$ (BBSC) can be found in our prior studies [24,25].

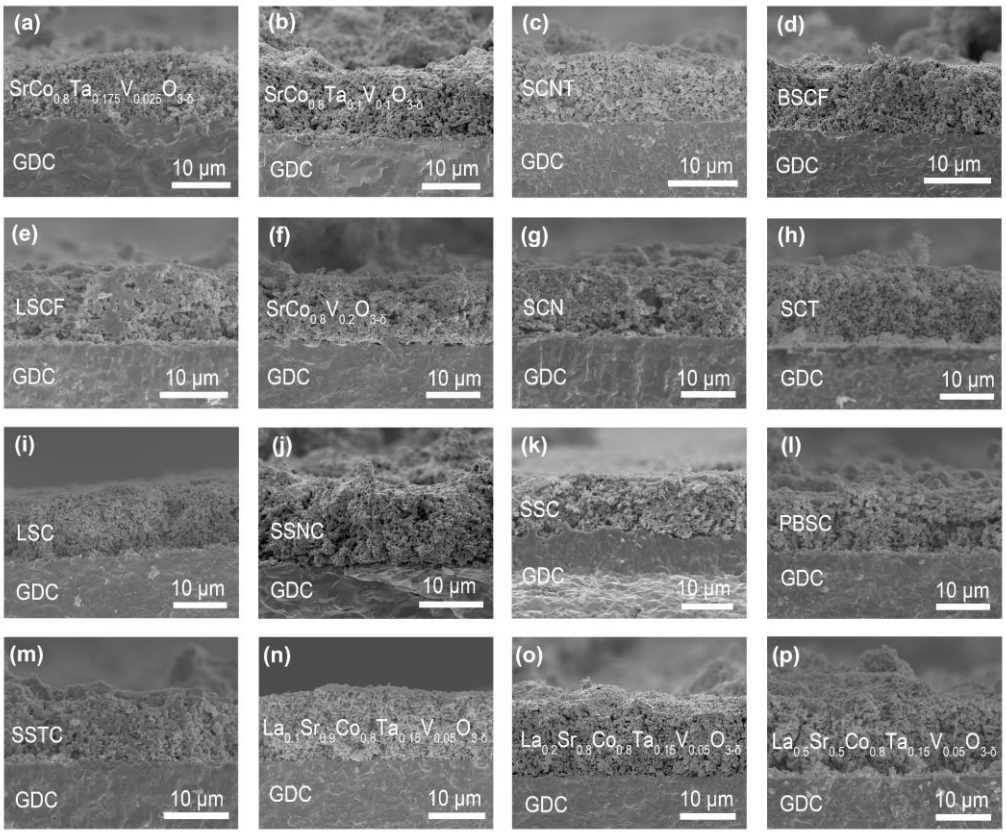

Supplementary Fig. S9 SEM cross-section images of representative symmetrical cells with different cathodes: (**a**) $SrCo_{0.8}Ta_{0.175}V_{0.025}O_{3-\delta}$ (SCTV0.175), (**b**) $SrCo_{0.8}Ta_{0.1}V_{0.1}O_{3-\delta}$ (SCTV0.1), (**c**) $SrCo_{0.8}Nb_{0.1}Ta_{0.1}O_{3-\delta}$ (SCNT), (**d**) $Ba_{0.5}Sr_{0.5}Co_{0.8}Fe_{0.2}O_{3-\delta}$ (BSCF), (**e**) $La_{0.6}Sr_{0.4}Co_{0.8}Fe_{0.2}O_{3-\delta}$ (LSCF), (**f**) $SrCo_{0.8}V_{0.2}O_{3-\delta}$, (**g**) $SrCo_{0.8}Nb_{0.2}O_{3-\delta}$ (SCN), (**h**) $SrCo_{0.8}Ta_{0.2}O_{3-\delta}$ (SCT), (**i**) $La_{0.6}Sr_{0.4}CoO_{3-\delta}$ (LSC), (**j**) $SrSc_{0.175}Nb_{0.025}Co_{0.8}O_{3-\delta}$ (SSNC), (**k**) $SrSc_{0.2}Co_{0.8}O_{3-\delta}$ (SSC), (**l**) $PrBa_{0.5}Sc_{0.5}Co_2O_{5+x}$ (PBSC), (**m**) $SrSc_{0.175}Ta_{0.025}Co_{0.8}O_{3-\delta}$ (SSTC), (**n**) $La_{0.1}Sr_{0.9}Co_{0.8}Ta_{0.15}V_{0.05}O_{3-\delta}$ (LSCTV0.1), (**o**) $La_{0.2}Sr_{0.8}Co_{0.8}Ta_{0.15}V_{0.05}O_{3-\delta}$ (LSCTV0.2), and (**p**) $La_{0.5}Sr_{0.5}Co_{0.8}Ta_{0.15}V_{0.05}O_{3-\delta}$ (LSCTV0.5).

Supplementary Note 4:

The GDC was used as the electrolyte, and the thickness of oxide layers was adjusted to about 10 μm on both sides of the electrolyte.

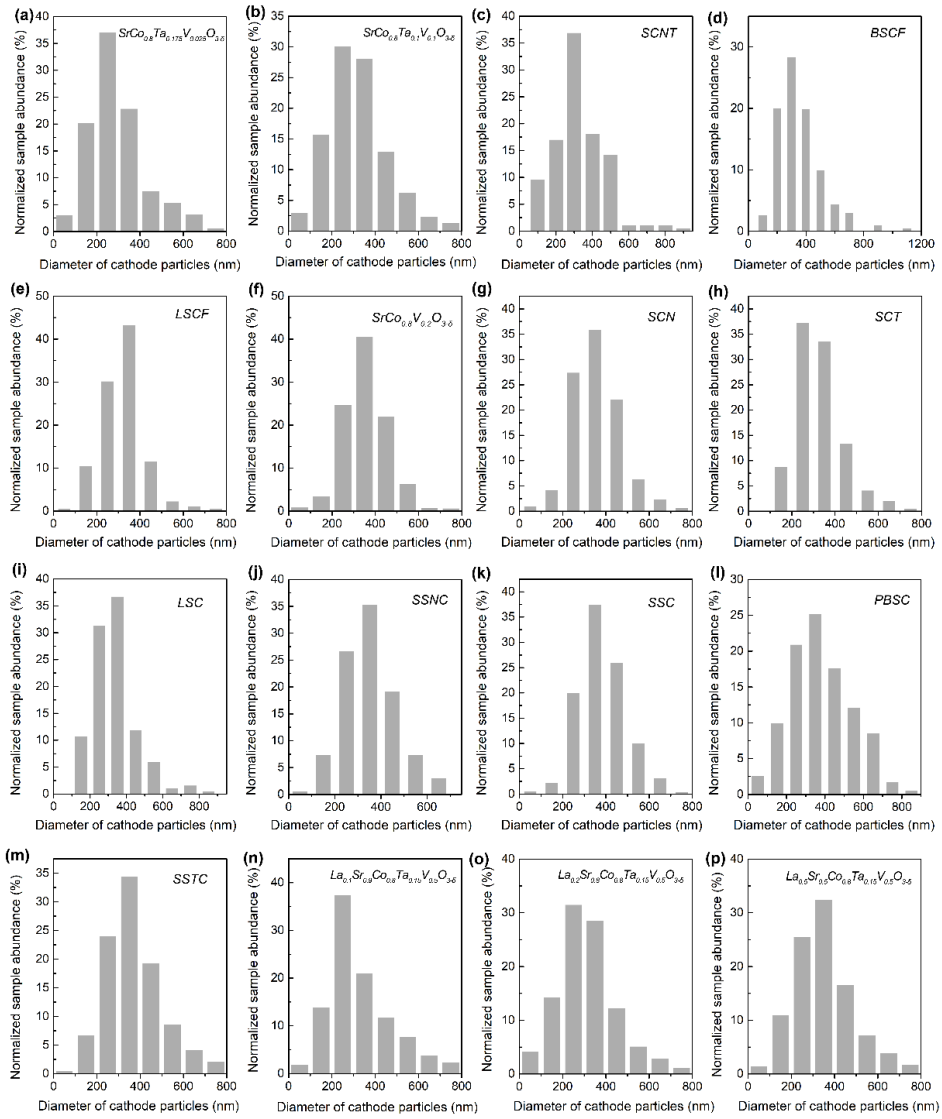

Supplementary Fig. S10 Statistics of particle size for the cathode materials: (**a**) $SrCo_{0.8}Ta_{0.175}V_{0.025}O_{3-\delta}$ (SCTV0.175), (**b**) $SrCo_{0.8}Ta_{0.1}V_{0.1}O_{3-\delta}$ (SCTV0.1), (**c**) $SrCo_{0.8}Nb_{0.1}Ta_{0.1}O_{3-\delta}$ (SCNT), (**d**) $Ba_{0.5}Sr_{0.5}Co_{0.8}Fe_{0.2}O_{3-\delta}$ (BSCF), (**e**) $La_{0.6}Sr_{0.4}Co_{0.8}Fe_{0.2}O_{3-\delta}$ (LSCF), (**f**) $SrCo_{0.8}V_{0.2}O_{3-\delta}$, (**g**) $SrCo_{0.8}Nb_{0.2}O_{3-\delta}$ (SCN), (**h**) $SrCo_{0.8}Ta_{0.2}O_{3-\delta}$ (SCT), (**i**) $La_{0.6}Sr_{0.4}CoO_{3-\delta}$ (LSC), (**j**) $SrSc_{0.175}Nb_{0.025}Co_{0.8}O_{3-\delta}$ (SSNC), (**k**) $SrSc_{0.2}Co_{0.8}O_{3-\delta}$ (SSC), (**l**) $PrBa_{0.5}Sc_{0.5}Co_2O_{5+x}$ (PBSC), (**m**) $SrSc_{0.175}Ta_{0.025}Co_{0.8}O_{3-\delta}$ (SSTC), (**n**) $La_{0.1}Sr_{0.9}Co_{0.8}Ta_{0.15}V_{0.05}O_{3-\delta}$ (LSCTV0.1), (**o**) $La_{0.2}Sr_{0.8}Co_{0.8}Ta_{0.15}V_{0.05}O_{3-\delta}$ (LSCTV0.2), and (**p**) $La_{0.5}Sr_{0.5}Co_{0.8}Ta_{0.15}V_{0.05}O_{3-\delta}$ (LSCTV0.5).

Supplementary Note 5:

The particle diameters of the cathode materials in symmetrical cells are mostly between 50-800 nm. The average particle size is commonly 250-350 nm for all materials.

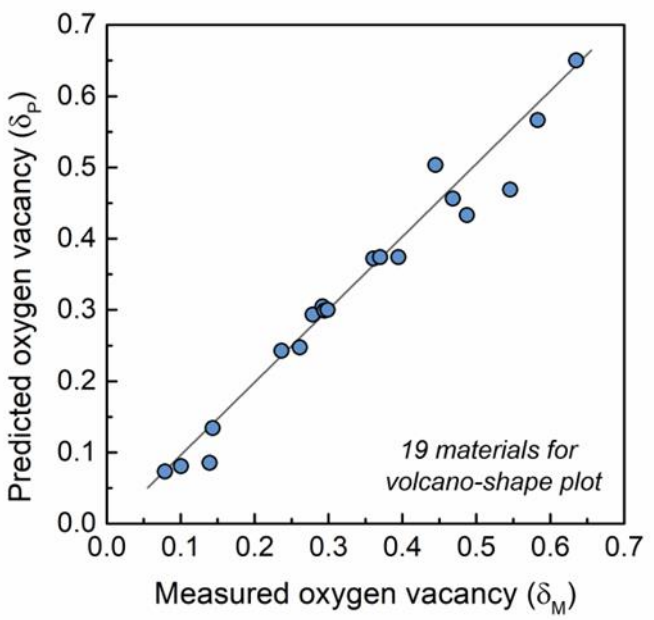

Supplementary Fig. S11 Linear relationship between measured and predicted oxygen vacancy for perovskite oxides synthesized and tested in this work.

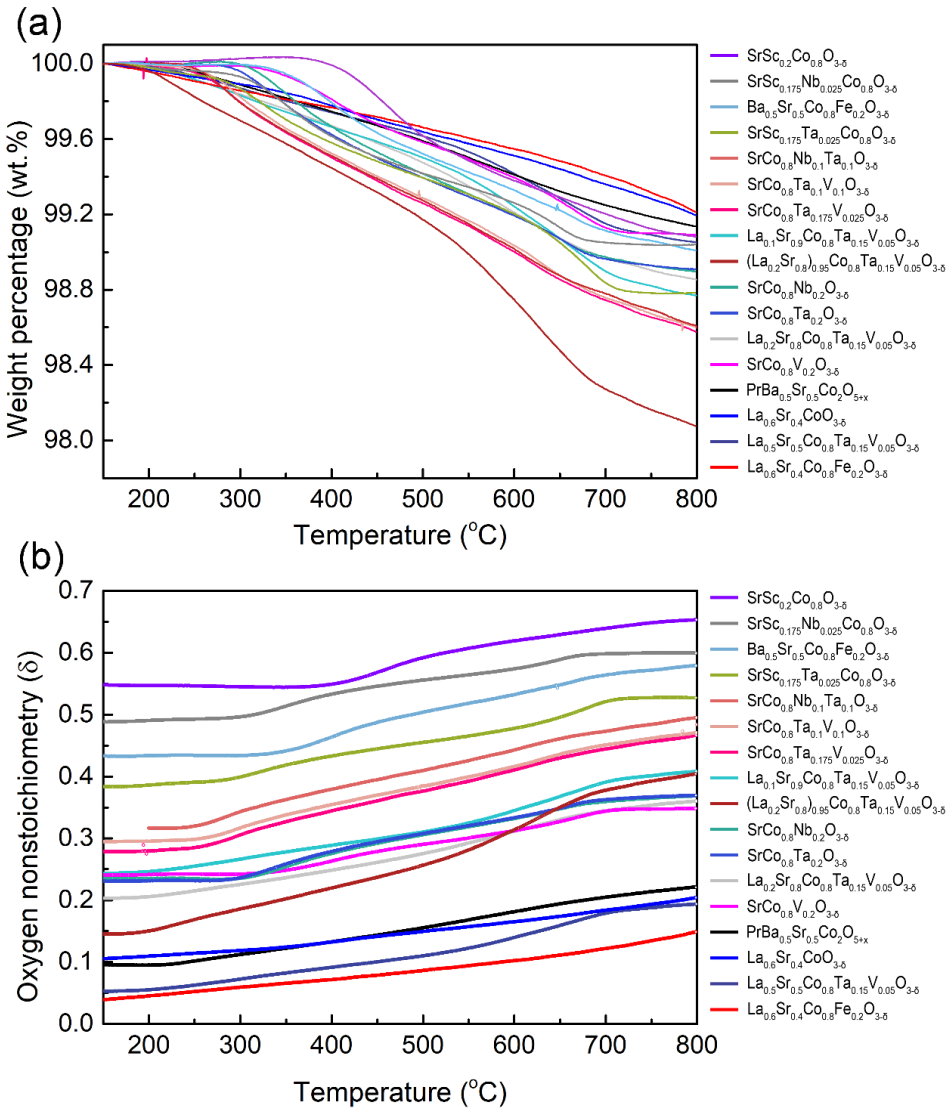

Supplementary Fig. S12 (**a**) TG analysis and (**b**) oxygen nonstoichiometry for various perovskite-type oxides from 150 °C to 800 °C. The values of δ at the very beginning point are determined from titration, and a higher δ value means higher concentrations of oxygen vacancies in the oxides.

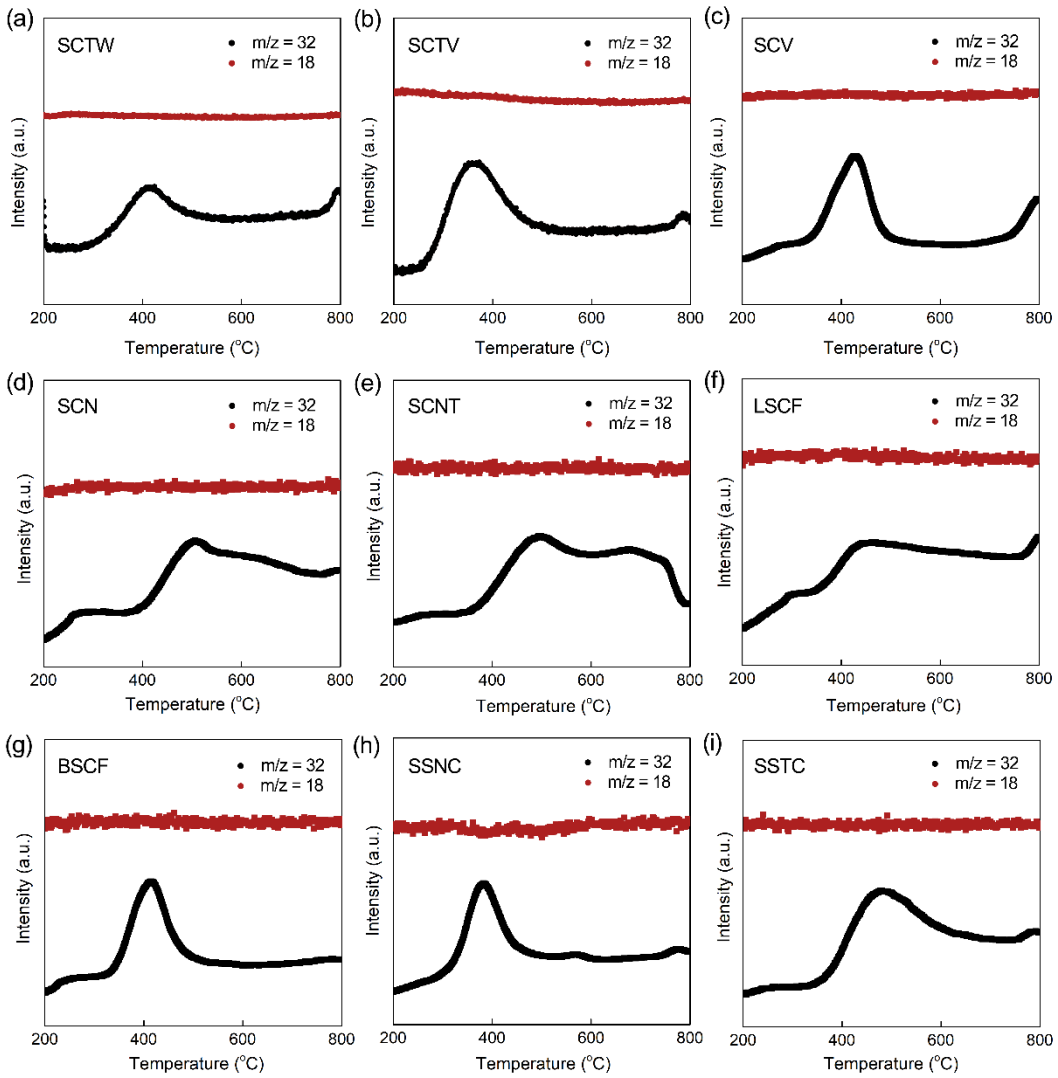

Supplementary Fig. S13 TPD-MS analysis tested from 200 – 800 °C for (**a**) SCTW, (**b**) SCTV, (**c**) SCV, (**d**) SCN, (**e**) SCNT, (**f**) LSCF, (**g**) BSCF, (**h**) SSNC, and (**i**) SSTC oxides. No peak for m/z = 18 (red) can be observed, indicating that there is no significant hydration step taking place during tests for all materials.

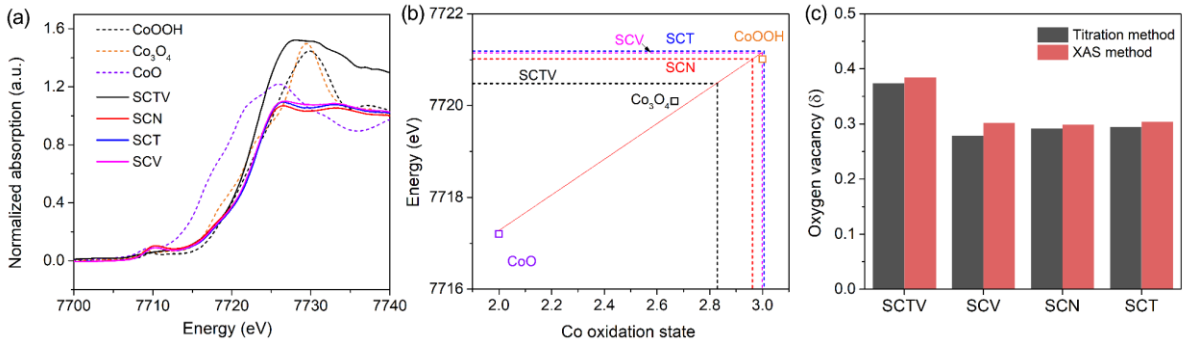

Supplementary Fig. S14 (**a**) Co K-edge XANES data of SCTV (black line), SCN (red line), SCT (blue line), and SCV (pink line) and standards for CoOOH (black, dashed line), Co_3O_4 (orange, dashed line), CoO (purple, dashed line). Before testes, SCTV, SCN, SCT, and SCV were quenched at 450 °C for 2 h and then sealed in Ar gas. We used the energy position at ordinate 0.6 to compare the oxidation states of cobalt in oxides. (**b**) Co oxidation states calculated from the absorption edge shift in XANES data of SCTV, SCN, SCT, and SCV. (**c**) Comparison in oxygen vacancy between titration method and XAS method for SCTV, SCN, SCT, and SCV.

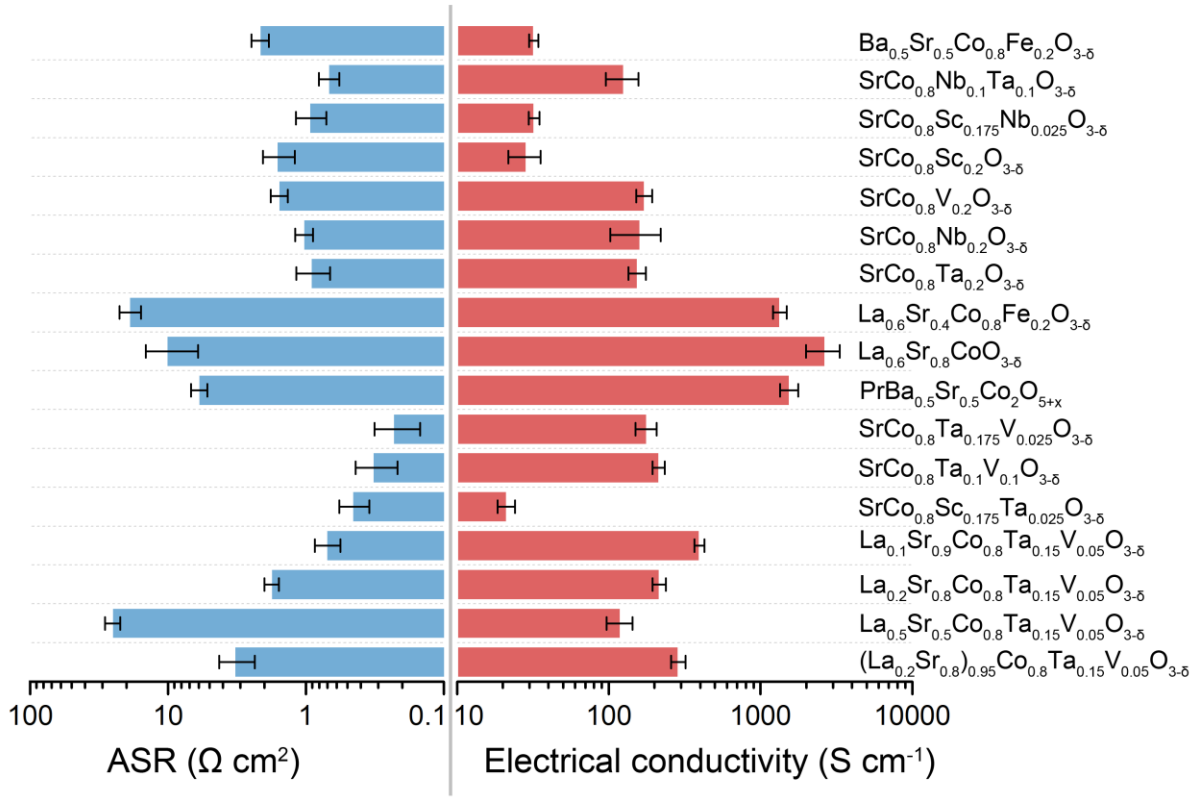

Supplementary Fig. S15 Electrical conductivity comparison of various perovskite-type oxides at 450 °C. All mean values ± S.D. of ASR and electrical conductivity were obtained after three times repetition.

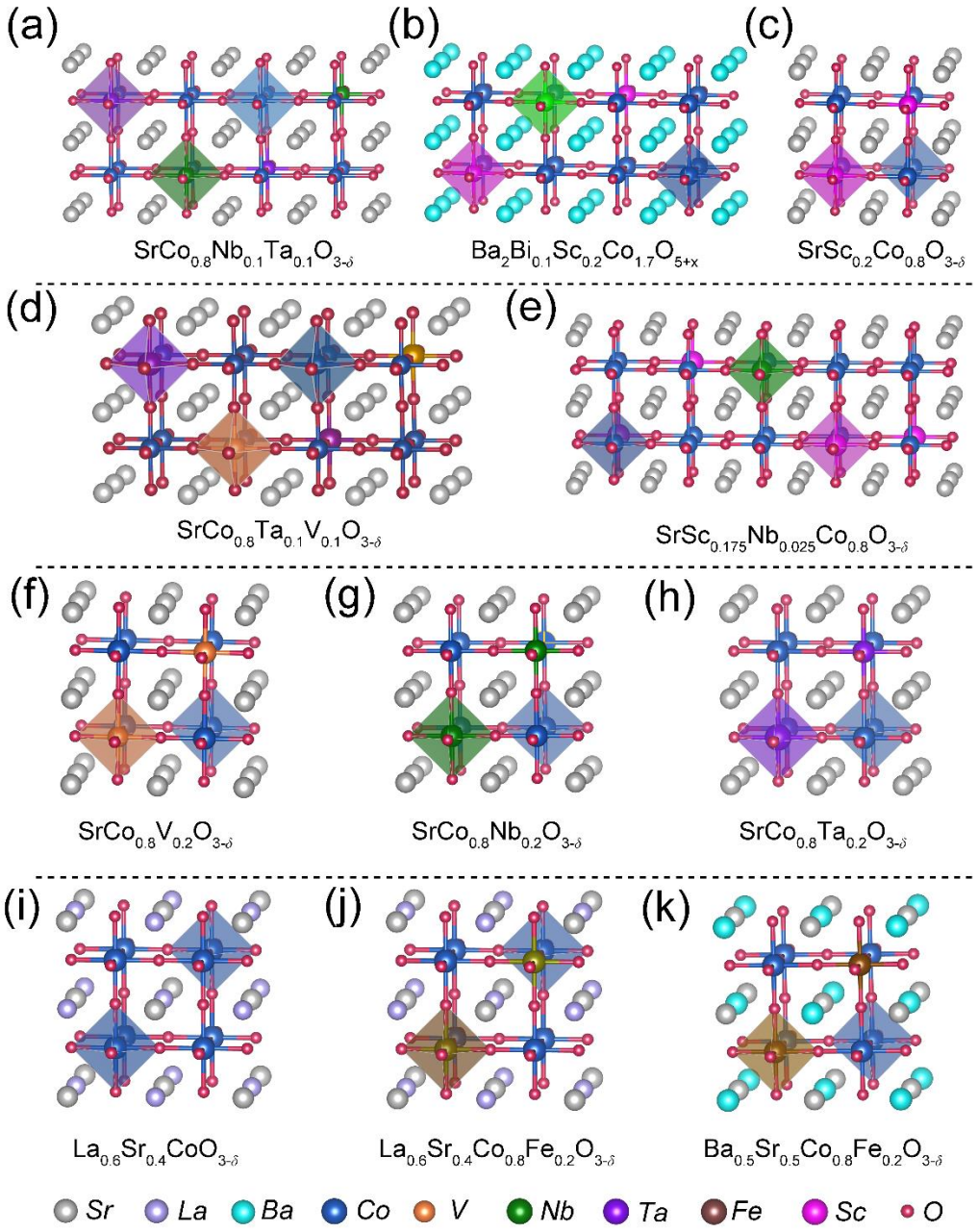

Supplementary Fig. S16 Optimized models with lowest total energies: (**a**) $SrCo_{0.8}Nb_{0.1}Ta_{0.1}O_{3-\delta}$ (SCNT), (**b**) $Ba_2Bi_{0.1}Sc_{0.2}Co_{1.7}O_{5+x}$ (BBSC), (**c**) $SrSc_{0.2}Co_{0.8}O_{3-\delta}$ (SSC), (**d**) $SrCo_{0.8}Ta_{0.1}V_{0.1}O_{3-\delta}$ (SCTV0.1), (**e**) $SrSc_{0.175}Nb_{0.025}Co_{0.8}O_{3-\delta}$ (SSTC), (**f**) $SrCo_{0.8}V_{0.2}O_{3-\delta}$, (**g**) $SrCo_{0.8}Nb_{0.2}O_{3-\delta}$ (SCN), (**h**) $SrCo_{0.8}Ta_{0.2}O_{3-\delta}$ (SCT), (**i**) $La_{0.6}Sr_{0.4}CoO_{3-\delta}$ (LSC), (**j**) $La_{0.6}Sr_{0.4}Co_{0.8}Fe_{0.2}O_{3-\delta}$ (LSCF), (**k**) $Ba_{0.5}Sr_{0.5}Co_{0.8}Fe_{0.2}O_{3-\delta}$ (BSCF).

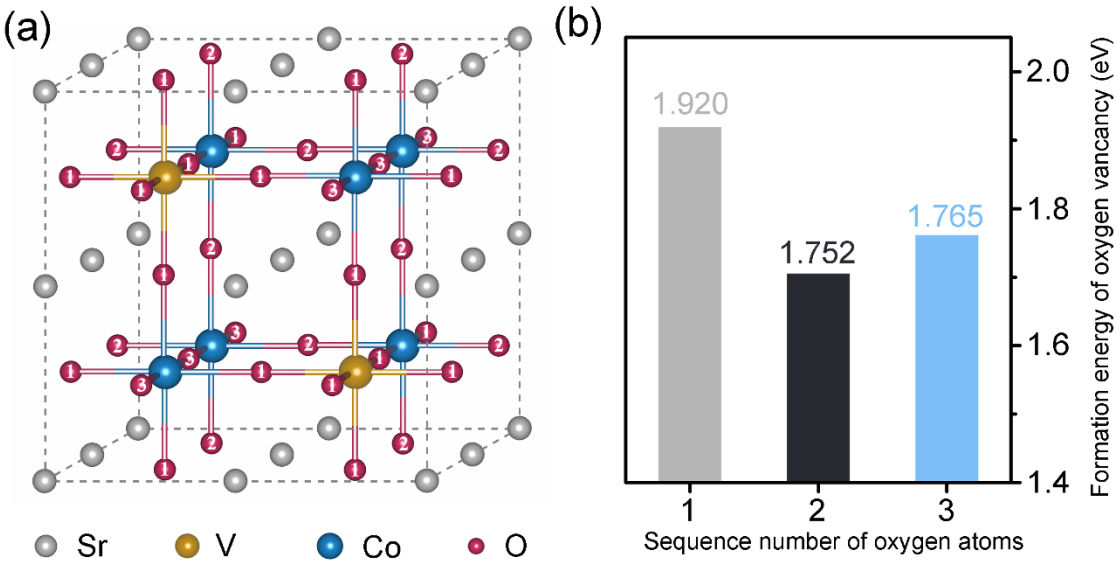

Supplementary Fig. S17 Formation energy of oxygen vacancy for representative SCV oxide. (**a**) Oxygen species (i.e., O1, O2, and O3) in SCV perovskite cell with face diagonal distribution of V dopant, (**b**) formation energies of oxygen vacancy from O1, O2, and O3.

Supplementary Note 6:

The lowest formation energy of oxygen vacancy is 1.752 eV over O2. The results demonstrate that the oxygen vacancy formation occurs most likely around cobalt ions that are far away from dopant ions. Similarly, other formation energies of oxygen vacancy are 1.591 eV for SCTV, 1.516 eV for 1.380 eV for SCNT, 1.593 eV for SCN, 1.669 eV for SCT, 1.215 eV for BSCF, 2.236 eV for LSCF, 0.922 eV for BBSC, 2.623 eV for LSC, and 0.8535 eV for SSC.

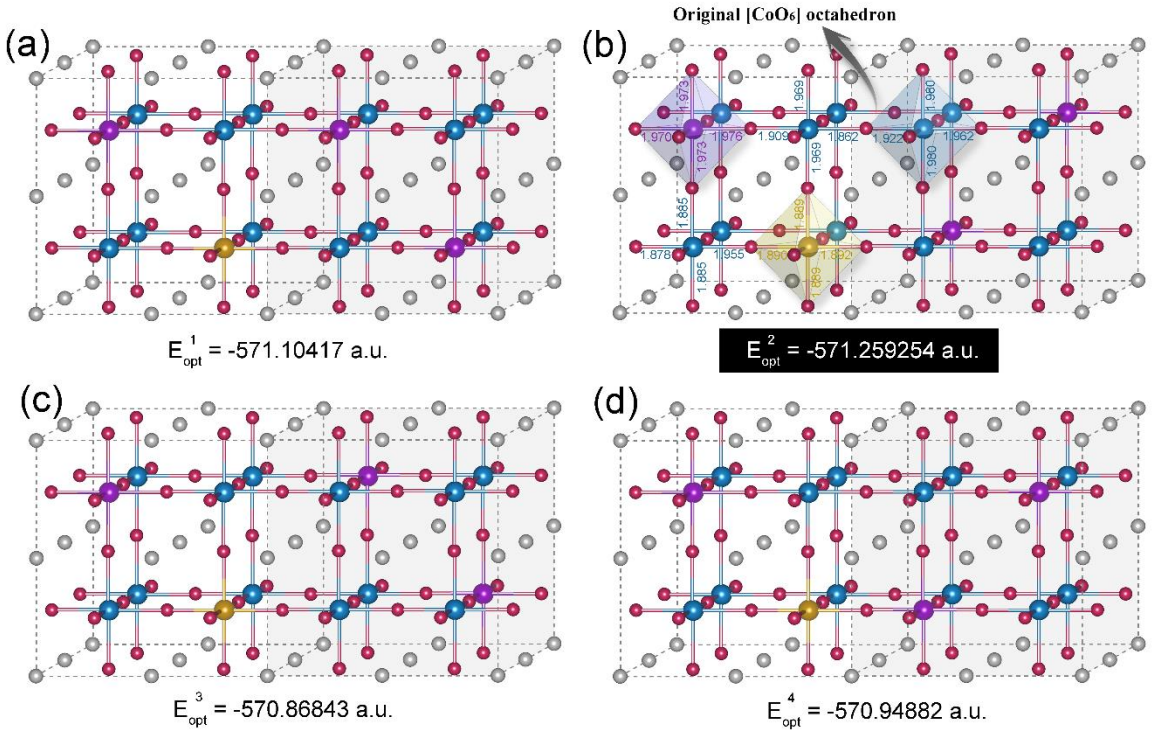

Supplementary Fig. S18 Model optimization of different SCTV lattice structures with (**a, b**) face diagonal distribution, (**c**) body diagonal distribution, and (**d**) neighbouring distribution of Ta and V dopants over the interface of two 2×2×2 monomer cells.

Supplementary Note 7:

To obtain more kinds of oxygen in different circumstances, the Ta and V dopants are commonly faced diagonal distribution in each monomer cell. Low total energy indicates a stable structure. Thus, the (**b**) structure is considered to be the most stable SCTV lattice structure because of the lowest structural energy of -571.259254 a.u.

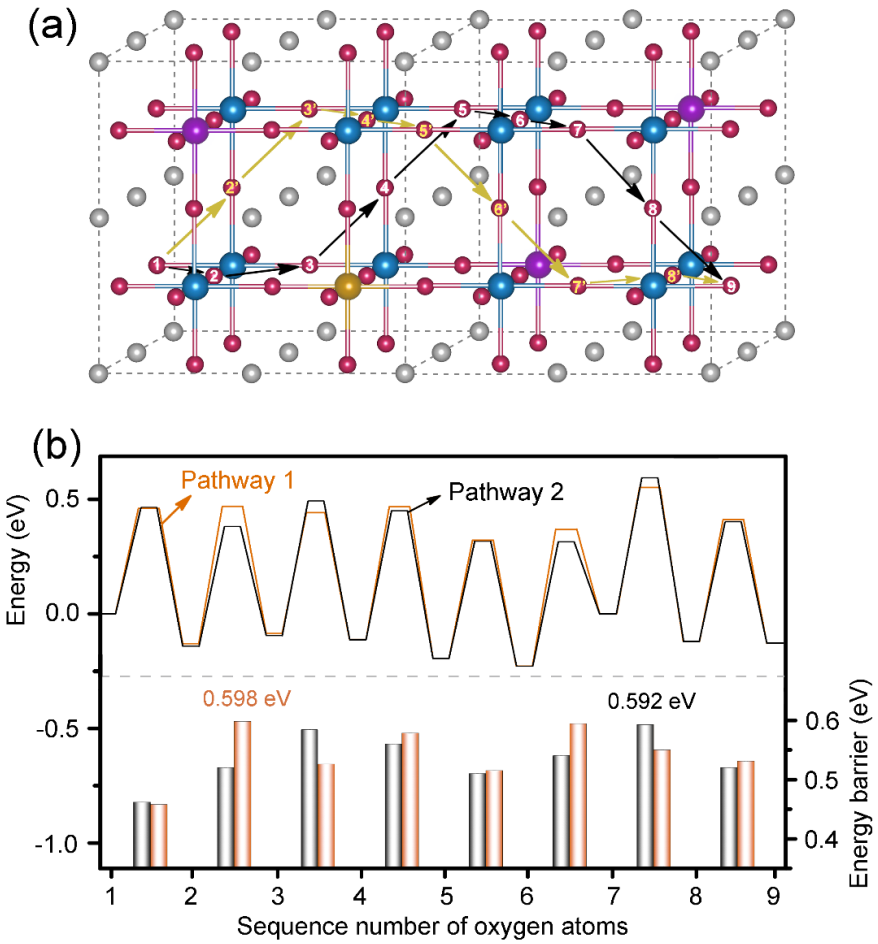

Supplementary Fig. S19 Energy barriers of oxygen-ion mobility for representative STVC oxide. (**a**) Possible pathways of oxygen-ion migration in SCTV with a principle of avoiding (TaO_6) and (VO_6) octahedrons as much as possible. (**b**) Energy barriers of each oxygen-ion migration transition state.

Supplementary Note 8:

Pathway 2 was selected as a better way to migrate oxygen-ion according to relatively lower energy barriers. The highest energy barrier in a pathway is normally the hardest step which rate-limits the oxygen-ion migration efficiency, such as 0.592 eV in pathway 2. Other pathways that are near to Ta or V dopants are not considered because their formation energies of oxygen vacancies should be generally high. Similarly, other energy barriers of oxygen-ion mobility are 0.680 eV for SCNT, 0.421 eV for SCV, 0.491 eV for SCN, 0.522 eV for SCT, 0.708 eV for BSCF, 0.310 eV for LSCF, 0.719 eV for BBSC, 0.430 eV for LSC, and 0.631 eV for SSC.

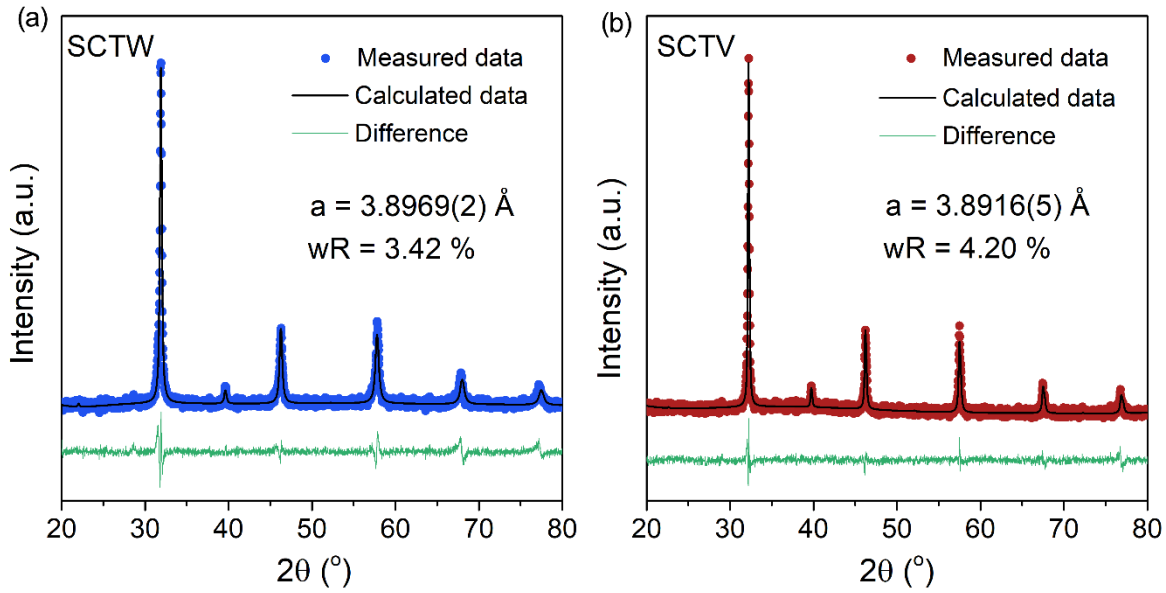

Supplementary Fig. S20 XRD patterns of (**a**) SCTW and (**b**) SCTV perovskites.

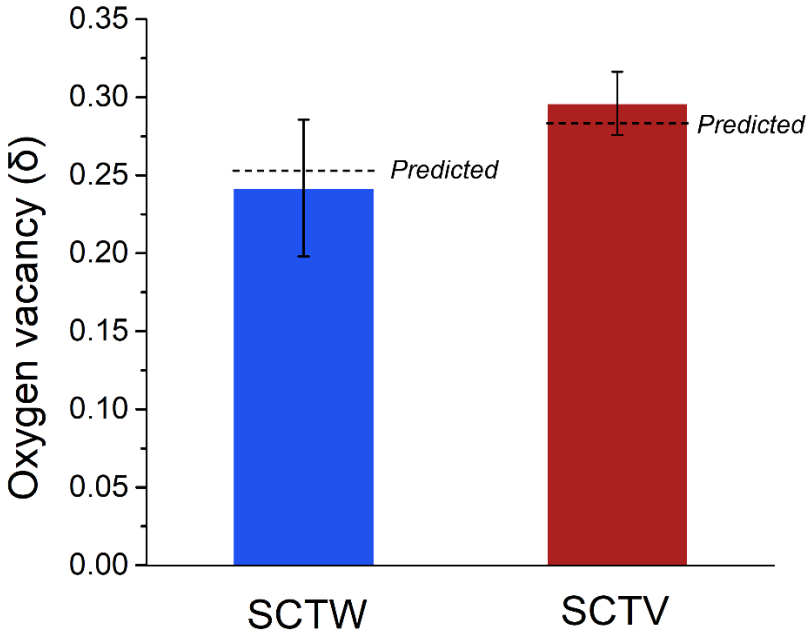

Supplementary Fig. S21 Mean values ± S.D. of oxygen vacancy for SCTW and SCTV perovskites at 25 °C. The measured results were obtained from the titration method and the predicted results were calculated from machine learning. The oxygen vacancy measurements were repeated for three times.

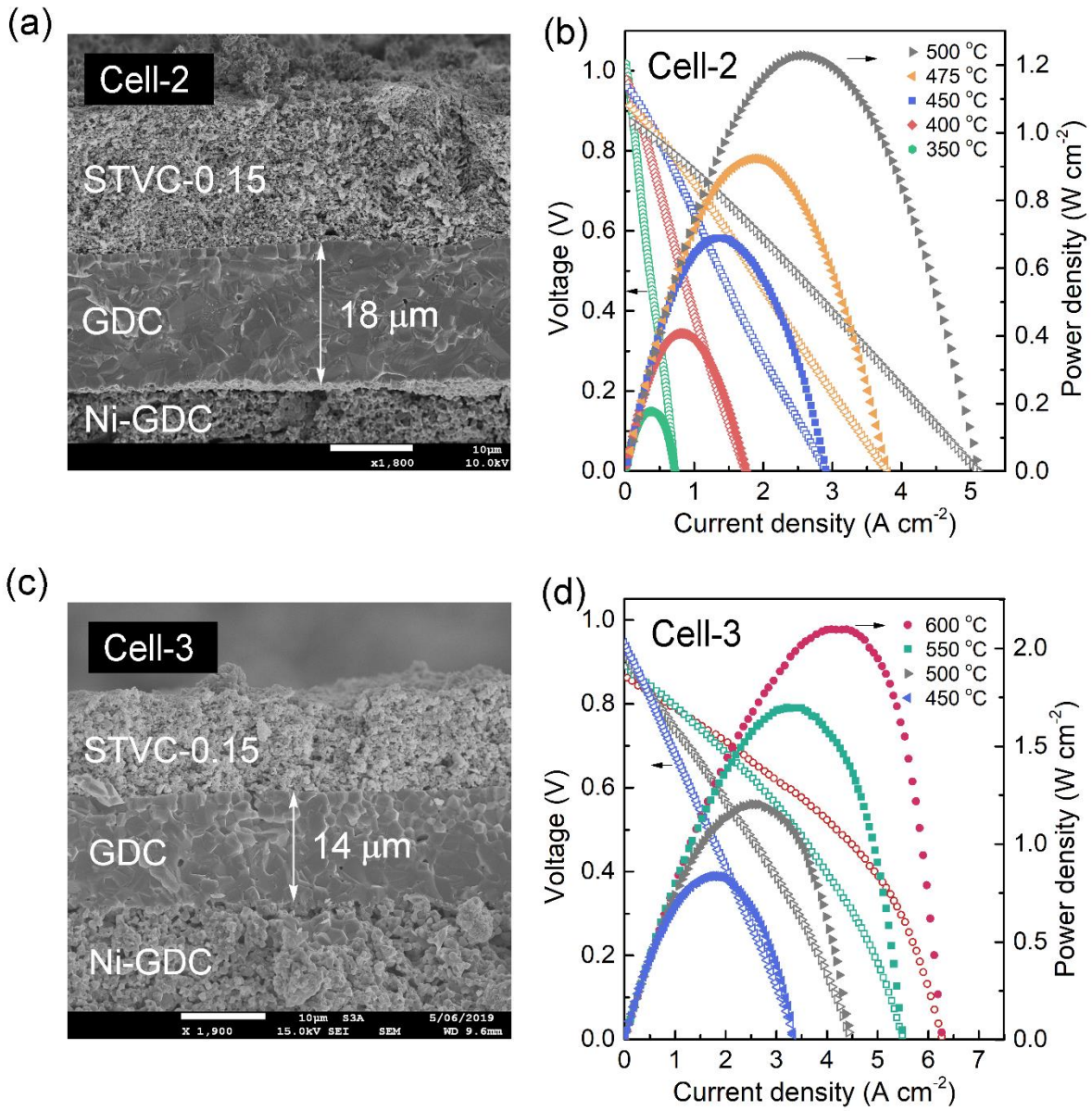

Supplementary Fig. S22 (**a**) Cross-sectional SEM image and (**b**) Voltage-current density curves and power densities of STVC catalyzed single-cell-2 (i.e., Cell-2). (c) Cross-sectional SEM image and (**d**) Voltage-current density curves and power densities of STVC catalyzed single-cell-3 (i.e., Cell-3).

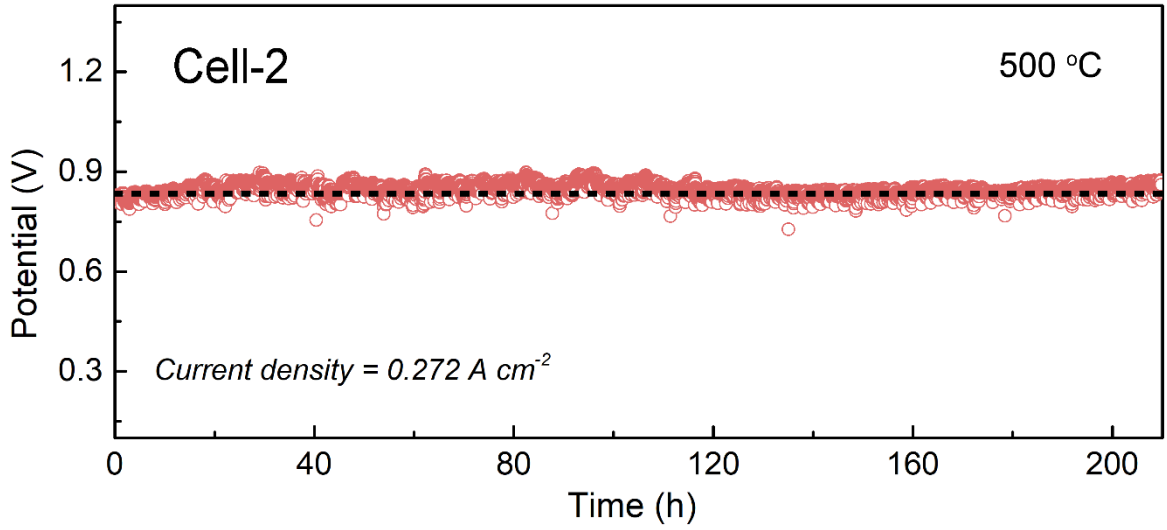

Supplementary Fig. S23 The stability of Cell-2 tested in synthetic air (O_2 balanced with N_2, without CO_2), without thermal cycling.

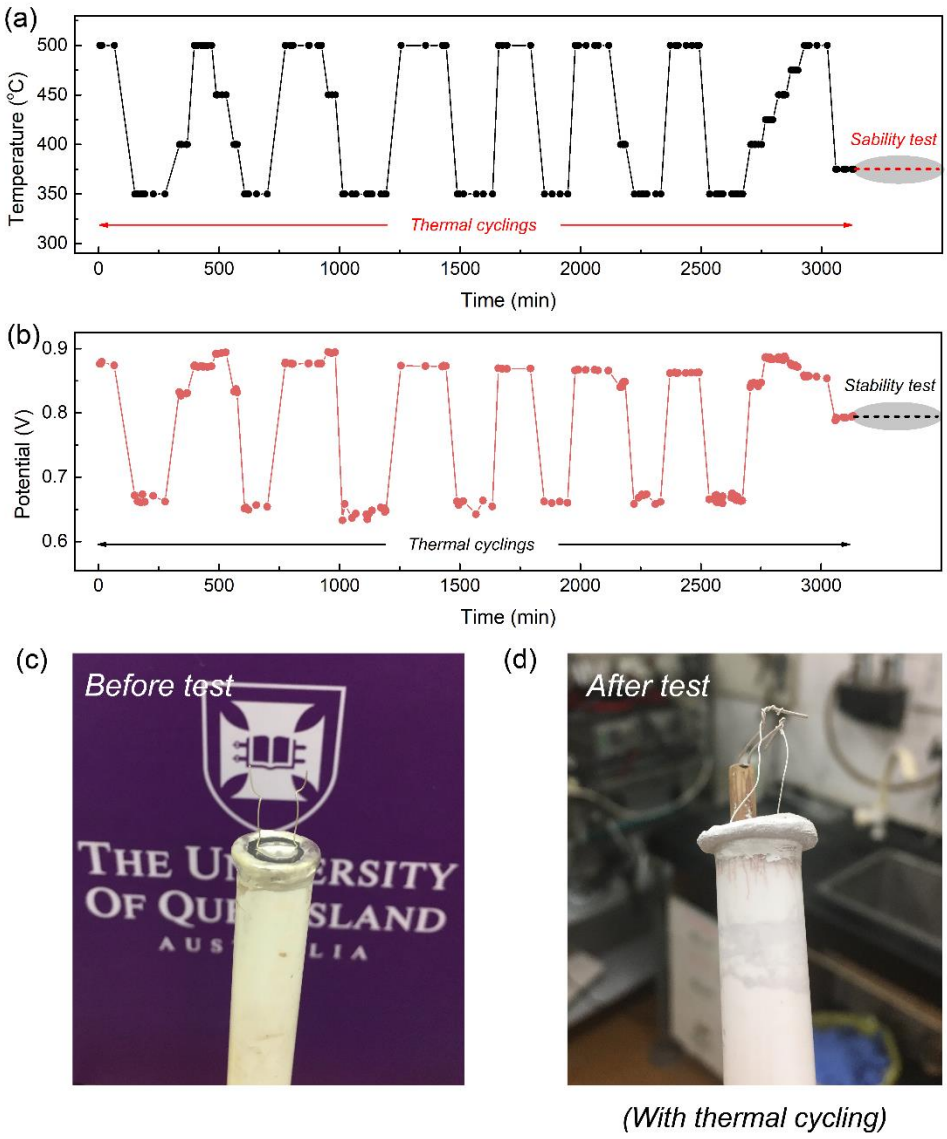

Supplementary Fig. S24 Cell-1 for short-term stability test with thermal cycling: (**a**) Temperature changes with time, (**b**) Potential changes with time, and the cell appearance (**c**) before and (**d**) after test

Supplementary Note 9:

Before the stability test, several fast thermal cycling (from 350 °C to 500 °C with a ramping time of 15 °C min^{-1}) were conducted to determine the performance of Cell-1. After the test, the dense silver seal became a soft and porous silver material, which can hardly seal up the H_2 in the pipe.

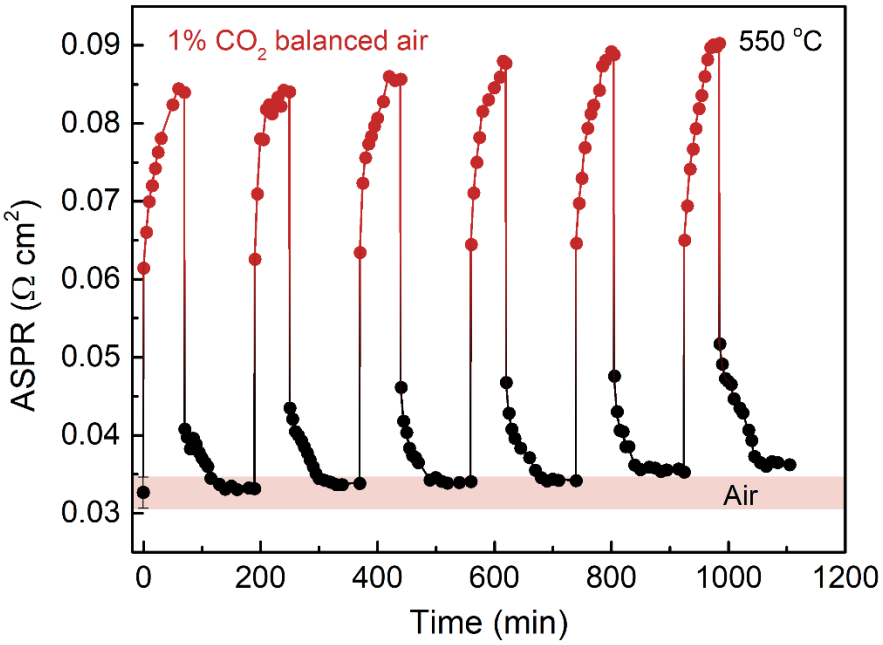

Supplementary Fig. S25 CO_2 resistance test of SCTV cathode material at 550 °C

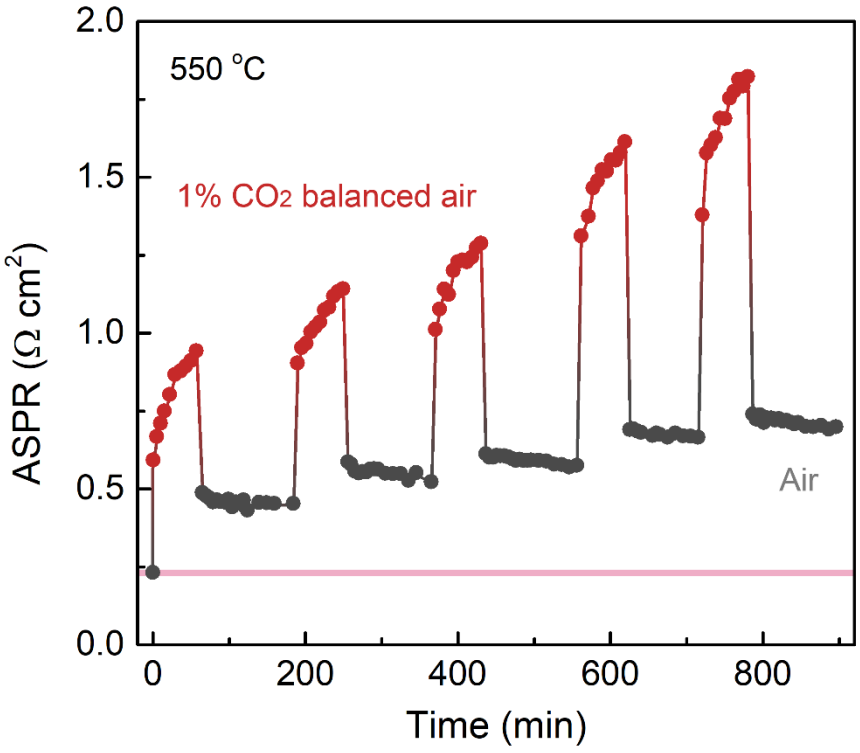

Supplementary Fig. S26 CO_2 resistance test of benchmark BSCF cathode material at 550 °C

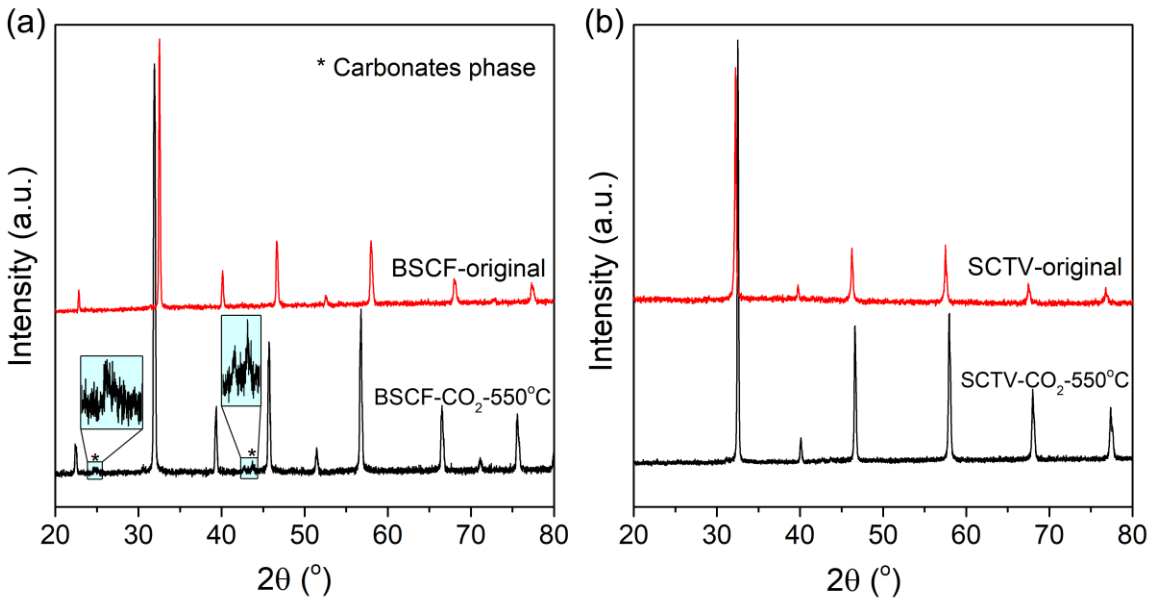

Supplementary Fig. S27 XRD patterns for (**a**) BSCF and (**b**) SCTC before and after CO_2 treatments at 550 °C

2. Supplementary table

Supplementary Table S1 Lattice parameter of the perovskite oxides compared to those in references

Materials	Lattice parameter (Å)	References
$Ba_{0.5}Sr_{0.5}Co_{0.8}Fe_{0.2}O_{3-\delta}$	3.9862(3)	*J. Solid State Chem.*, **18**, 576-586 (2008).
$SrCo_{0.8}Nb_{0.1}Ta_{0.1}O_{3-\delta}$	3.9066(1)	*Nat. Commun.*, **8**, 13990 (2017).
$SrSc_{0.175}Nb_{0.025}Co_{0.8}O_{3-\delta}$	3.904	*Angew. Chem. Int. Ed.*, **52**, 14036-14040 (2013)
$SrCo_{0.8}Nb_{0.1}Ta_{0.1}O_{3-\delta}$	3.90402(3)	*Adv. Funct. Mater.*, **33**, 2210496 (2023).
$SrCo_{0.8}Nb_{0.2}O_{3-\delta}$	3.90357(3)	*Adv. Funct. Mater.*, **33**, 2210496 (2023).
$SrCo_{0.8}Ta_{0.2}O_{3-\delta}$	3.90820(4)	*Adv. Funct. Mater.*, **33**, 2210496 (2023).
$Sr_{0.95}Ag_{0.05}Nb_{0.1}Co_{0.9}O_{3-\delta}$	3.8733	*Nano letters*, **16**, 512-518 (2016).
$SrCo_{0.8}V_{0.2}O_{3-\delta}$	3.8647(7)	This work
$SrCo_{0.8}Nb_{0.2}O_{3-\delta}$	3.8983(6)	This work
$SrCo_{0.8}Ta_{0.2}O_{3-\delta}$	3.9053(6)	This work
$SrSc_{0.175}Ta_{0.025}Co_{0.8}O_{3-\delta}$	3.9119(4)	This work
$Ba_{0.5}Sr_{0.5}Co_{0.8}Fe_{0.2}O_{3-\delta}$	3.9144(3)	This work
$SrCo_{0.8}Ta_{0.16}W_{0.04}O_{3-\delta}$	3.8969(2)	This work
$SrCo_{0.8}Ta_{0.1}V_{0.1}O_{3-\delta}$	3.8764(3)	This work
$SrCo_{0.8}Ta_{0.15}V_{0.05}O_{3-\delta}$	3.8916(5)	This work
$SrCo_{0.8}Ta_{0.175}V_{0.025}O_{3-\delta}$	4.0759(5)	This work
$(La_{0.2}Sr_{0.8})_{0.95}Co_{0.8}Ta_{0.15}V_{0.05}O_{3-\delta}$	3.8501(3)	This work
$La_{0.1}Sr_{0.9}Co_{0.8}Ta_{0.15}V_{0.05}O_{3-\delta}$	3.8904(2)	This work
$La_{0.2}Sr_{0.8}Co_{0.8}Ta_{0.15}V_{0.05}O_{3-\delta}$	3.8872(1)	This work
$SrSc_{0.175}Ta_{0.025}Co_{0.8}O_{3-\delta}$	3.9349(5)	This work
$SrCo_{0.8}Nb_{0.1}Ta_{0.1}O_{3-\delta}$	3.90147(9)	This work

Supplementary Table S2 Laboratory XRD refinement details for SCTV

Atom	Site Multiplicity	*x*	*y*	*z*	Occupancy	U_{iso} (Å^2)
SCTV, *a* = 3.8880(5) Å, *Pm*$\bar{3}$*m*, phase fraction 100%						
Sr	1	0.5	0.5	0.5	1.03(8)	0. 017(9)
V	1	0	0	0	0.05(4)	0.02(1)[a]
Co	1	0	0	0	0.800(2)	0.02(1)[a]
Ta	1	0	0	0	0.15(4)	0.02(1)[a]
O	3	0.5	0	0	0.9[b]	0.01[c]
Goodness of fit (GOF) = 1.16						
Weighted profile R-factor (wR) = 4.20%						

[a] Atomic displacement parameters constrained to be equal for atoms at the same site.

[b] Occupancy is fixed to the titration results

[c] Atomic displacement fixed to the literature value [26].

Supplementary Table S3 Laboratory XRD refinement details for SCTW

Atom	Site Multiplicity	*x*	*y*	*z*	Occupancy	U_{iso} (Å^2)
SCTW, *a* = 3.8894(2) Å, *Pm*$\bar{3}$*m*, phase fraction 100%						
Sr	1	0.5	0.5	0.5	1.01(2)	0. 009(2)
Co	1	0	0	0	0.77(2)	0.008(3)[a]
Ta/W[b]	1	0	0	0	0.23(2)	0.008(3)[a]
O	3	0.5	0	0	0.9[c]	0.01[d]
Goodness of fit (GOF) = 1.37						
Weighted profile R-factor (wR) = 3.42%						

[c] Atomic displacement parameters constrained to be equal for atoms at the same site.

[b] Ta and W are indistinguishable in XRD and combined.

[c] Occupancy is fixed to the titration results

[d] Atomic displacement fixed to the literature value [26].

Supplementary Table S4 Performance comparison for different cathode materials based on relative symmetrical cells

Cathode		Electrolyte	ASRs in symmetrical cells (Ω cm^2)							Ea (kJ mol^{-1})	Source
Name [a]	Thickness		400 °C	450 °C	500 °C	550 °C	600 °C	650 °C	700 °C		
SCTV	10	GDC10 [b]	0.509	0.165	0.0664	0.0327	0.0185	0.0108	0.0077	76.2	This work
SCTW	10	GDC10	1.037	0.265	0.0952	0.0391	0.0211	0.0111	0.0079	88.9	This work
SCNT	10	SDC [c]/GDC10		0.683	0.307	0.0615	0.0252	0.0141	0.0076	103	Li, 2017 [19]
BBSC	——	SDC		5.53	1.81	0.612	0.223	0.088	0.038	116	Zhou, 2011 [25]
SSTC	15	SDC		——	0.221	0.083	0.031	0.012	0.0053	117	Xu, 2019 [27]
SSNC	10	SDC		0.949	0.315	0.104	0.041	0.020	0.0098	108	Zhou, 2013 [28]
BSCF	20	SDC	8.75	2.01	0.645	0.219	0.0724	0.029	0.013	116	Shao, 2004 [12]
SANC	15	SDC		0.648	0.214	0.0848	0.0374	0.019	0.012	95	Zhu, 2015 [24]
PBSCF	30	SDC		——	0.783	0.320	0.131	0.062	0.033	100	Chen, 2018 [29]
SPN-A-PBC	——	CGO [d]		——	0.571	0.271	0.113	0.049	0.025	106	Lu, 2019 [30]
BCFY	7	SDC		——	0.43	0.1	0.03	0.014	——	126	He, 2017 [31]
BSFCu	15	GDC10		——	0.93	0.25	0.084	0.035	0.017	125	Yang, 2015 [32]
NBCaCO	10	GDC10		——	0.403	0.167	0.0656	0.0261	——	108	Yoo, 2014 [33]
LSCF fiber	10	SDC		——	——	1.085	0.433	0.188	0.1	106	Chen, 2017[34]
GBSCF	——	YSZ [e]		——	1.117	0.216	0.042	0.014	0.006	163	Kim, 2015 [35]
SBSCF-GDC	20	GDC10		——	0.607	0.203	0.081	0.0407	——	106	Jun, 2015 [36]

[a] Abbreviation: SCTV ($SrCo_{0.8}Ta_{0.15}V_{0.05}O_{3-\delta}$), SCTW ($SrCo_{0.8}Ta_{0.16}W_{0.04}O_{3-\delta}$), SCNT ($SrCo_{0.8}Nb_{0.1}Ta_{0.1}O_{3-\delta}$), BBSC ($Ba_2Bi_{0.1}Sc_{0.2}Co_{1.7}O_{6-x}$), SSTC ($SrSc_{0.175}Ta_{0.025}Co_{0.8}O_{3-\delta}$), SSNC ($SrSc_{0.175}Nb_{0.025}Co_{0.8}O_{3-\delta}$), BSCF ($Ba_{0.5}Sr_{0.5}Co_{0.8}Fe_{0.2}O_{3-\delta}$), SANC ($Sr_{0.95}Ag_{0.05}Nb_{0.1}Co_{0.9}O_{3-\delta}$), PBSCF

($PrBa_{0.5}Sr_{0.5}Co_{1.5}Fe_{0.5}O_{5+\delta}$), SPN-A-PBC ($PrBa_{0.94}Co_2O_{5+\delta}$), BCFY ($BaCo_{0.7}Fe_{0.22}Y_{0.08}O_{3-\delta}$), BSFCu ($Ba_{0.5}Sr_{0.5}Fe_{0.8}Cu_{0.1}Ti_{0.1}O_{3-\delta}$), NBCaCO ($NdBa_{1-x}Ca_xCo_2O_{5+\delta}$), LSCF ($(La_{0.6}Sr_{0.4})_{0.95}Co_{0.2}Fe_{0.8}O_{3+\delta}$) fiber, GBSCF ($GdBa_{0.5}Sr_{0.5}CoFeO_{5+\delta}$), and SBSCF ($SmBa_{0.5}Sr_{0.5}Co_{2-x}Fe_xO_{5+\delta}$)- GDC.

[b] $Gd_{0.1}Ce_{0.9}O_{1.95}$ (GDC10), [c] $Sm_{0.2}Ce_{0.8}O_{1.9}$ (SDC), [d] $Ce_{0.9}Gd_{0.1}O_{1.95}$ (CDG) and [e] Yttria-Stabilized Zirconia (YSZ)

Supplementary Table S5 Performance of representative SOFC and PCFC from prior literatures published after 2015. The fuel cells are all fuelled with H_2.

Type	Cathode (thickness)	Electrolyte (thickness)	Anode	Peak power density (W cm^{-2})				Source
				350 °C	400 °C	450 °C	500 °C	
SOFC	SCTV (18 μm)	GDC10 [a] (14 μm)	Ni-GDC10	0.19	0.45	0.85	1.36	This work
SOFC	$BaCo_{0.4}Fe_{0.4}Zr_{0.1}Y_{0.1}O_{3-\delta}$ (20 μm)	GDC20 [b] (10 μm)	Ni-GDC10	0.13	0.32	0.64	0.98	Duan, 2017 [37]
SOFC	$SrCo_{0.8}Nb_{0.1}Ta_{0.1}O_{3-\delta}$ (10 μm)	GDC10 [a] (14 μm)	Ni-GDC10			0.7	1.22	Li, 2017 [19]
SOFC	$PrBa_{0.5}Sr_{0.5}Co_2O_{5+\delta}$	GDC10 [a] (15 μm)	Ni-GDC10			0.36	0.62	Chen, 2016 [38]
SOFC	$Sr_{0.95}Ag_{0.05}Nb_{0.1}Co_{0.9}O_{3-\delta}$ (~15μm)	SDC [c] (11.8 μm)	Ni-SDC		0.327	0.629	1.106	Zhu, 2016 [24]
SOFC	$PrBaCo_2O_{5+x}$ (80 μm)	$BaZr_{0.8}Y_{0.2}O_{3-\delta}$ (15 μm)	Ni-$BaZr_{0.8}Y_{0.2}O_{3-\delta}$				0.292	Bi, 2018 [39]
SOFC	$Sm_{0.5}Sr_{0.5}CoO_{3-\delta}$ (80 μm)	$BaZr_{0.8}Y_{0.2}O_{3-\delta}$ (15 μm)	Ni-$BaZr_{0.8}Y_{0.2}O_{3-\delta}$				0.249	Bi, 2018 [39]
PCFC	$La_{0.6}Sr_{0.4}CoO_{3-\delta}$ (2 μm)	$BaZr_{0.85}Y_{0.15}O_{3-\delta}$ (2.5 μm)	Ni-$BaZr_{0.85}Y_{0.15}O_{3-\delta}$			0.342	0.457	Bae, 2017 [40]
PCFC	$Ba_{0.5}Sr_{0.5}Co_{0.8}Fe_{0.2}O_{3-\delta}$-$BaZr_{0.84}Y_{0.15}Cu_{0.01}O_{3-\delta}$	$BaCe_{0.55}Zr_{0.3}Y_{0.15}O_{3-\delta}$ (2.5 μm)	Ni-$BaCe_{0.55}Zr_{0.3}Y_{0.15}O_{3-\delta}$				0.35	Choi, 2019 [41]
PCFC	$Ba_{0.5}Sr_{0.5}Co_{0.8}Fe_{0.2}O_{3-\delta}$ (25 μm)	$BaCe_{0.55}Zr_{0.3}Y_{0.15}O_{3-\delta}$ (5 μm)	Ni-$BaCe_{0.55}Zr_{0.3}Y_{0.15}O_{3-\delta}$			~ 0.28	~ 0.54	An, 2018 [42]
PCFC	$BaCo_{0.4}Fe_{0.4}Zr_{0.1}Y_{0.1}O_{3-\delta}$ (30 μm)	Ni-$BaCe_{0.7}Zr_{0.1}Y_{0.1}Yb_{0.1}O_{3-\delta}$ (20 μm)	Ni-$BaCe_{0.7}Zr_{0.1}Y_{0.1}Yb_{0.1}O_{3-\delta}$	0.075	0.15	0.25	0.4	Duan, 2015 [43]
PCFC	$PrBa_{0.5}Sr_{0.5}Co_{1.5}Fe_{0.5}O_{5+\delta}$ (20 μm)	$BaZr_{0.4}Ce_{0.4}Y_{0.1}Yb_{0.1}O_3$ (15 μm)	Ni-$BaZr_{0.4}Ce_{0.4}Y_{0.1}Yb_{0.1}O_3$			~ 0.4	~ 0.56	Choi, 2018 [44]
PCFC	$PrBa_{0.5}Sr_{0.5}Co_{1.5}Fe_{0.5}O_{5+\delta}$ (~30 μm)	$BaZr_{0.1}Ce_{0.7}Y_{0.1}Yb_{0.1}O_{3-\delta}$ (~20 μm)	Ni-$BaZr_{0.1}Ce_{0.7}Y_{0.1}Yb_{0.1}O_{3-\delta}$				~ 0.45	Chen, 2018 [29]
SOFC	$Ba_{0.5}Sr_{0.5}Co_{0.8}Fe_{0.2}O_{3-\delta}$-GDC10 (~30 μm)	GDC10 [a] (~5 μm)	Ni-GDC10			~ 0.65	~ 1.23	Lee, 2014 [45]
SOFC	Porous platinum (60 nm)	Yttria-stabilized zirconia (80 nm)	Porous platinum (60 nm)		0.36	0.82	1.34	Chao, 2011 [46]

[a] $Gd_{0.1}Ce_{0.9}O_{1.95}$ (GDC10), [b] $Gd_{0.2}Ce_{0.8}O_{1.95}$ (GDC20) and [c] $Sm_{0.2}Ce_{0.8}O_{1.9}$ (SDC)

References

1 Goodenough, J. B. *Magnetism and the chemical bond* (Interscience Publishers, 1963).

2 Shannon, R. Revised effective ionic radii and systematic studies of interatomic distances in halides and chalcogenides. *Acta Crystallographica Section A* **32**, 751-767, (1976).

3 Pauling, L. The Sizes of Ions and the Structure of Ionic Crystals. *J. Am. Chem. Soc.* **49**, 765-790, (1927).

4 Matar, S. F., Campet, G. & Subramanian, M. A. Electronic properties of oxides: Chemical and theoretical approaches. *Prog. Solid State Chem.* **39**, 70-95, (2011).

5 Cheng, X. *et al.* Oxygen Evolution Reaction on Perovskites: A Multieffect Descriptor Study Combining Experimental and Theoretical Methods. *ACS Catalysis* **8**, 9567-9578, (2018).

6 Porokhin, S. V. *et al.* Mixed-Cation Perovskite $La_{0.6}Ca_{0.4}Fe_{0.7}Ni_{0.3}O_{2.9}$ as a Stable and Efficient Catalyst for the Oxygen Evolution Reaction. *ACS Catalysis* **11**, 8338-8348, (2021).

7 Pan, Y. *et al.* Direct evidence of boosted oxygen evolution over perovskite by enhanced lattice oxygen participation. *Nat. Commun.* **11**, 2002, (2020).

8 Mefford, J. T. *et al.* Water electrolysis on $La_{1-x}Sr_xCoO_{3-\delta}$ perovskite electrocatalysts. *Nat. Commun.* **7**, 11053, (2016).

9 Suntivich, J., May, K. J., Gasteiger, H. A., Goodenough, J. B. & Shao-Horn, Y. A Perovskite Oxide Optimized for Oxygen Evolution Catalysis from Molecular Orbital Principles. *Science* **334**, 1383-1385, (2011).

10 She, S. *et al.* Systematic Study of Oxygen Evolution Activity and Stability on $La_{1-x}Sr_xFeO_{3-\delta}$ Perovskite Electrocatalysts in Alkaline Media. *ACS Appl. Mater. Interfaces* **10**, 11715-11721, (2018).

11 Xu, X. *et al.* Co-doping Strategy for Developing Perovskite Oxides as Highly Efficient Electrocatalysts for Oxygen Evolution Reaction. *Advanced Science* **3**, 1500187, (2016).

12 Shao, Z. & Haile, S. M. A high-performance cathode for the next generation of solid-oxide fuel cells. *Nature* **431**, 170-173, (2004).

13 Yang, X. *et al.* Improving stability and electrochemical performance of $Ba_{0.5}Sr_{0.5}Co_{0.2}Fe_{0.8}O_{3-\delta}$ electrode for symmetrical solid oxide fuel cells by Mo doping. *J. Alloys Compd.* **831**, 154711, (2020).

14 Lin, Y. *et al.* Evaluation of $Ba_{0.5}Sr_{0.5}Co_{0.8}Fe_{0.2}O_{3-\delta}$ as a potential cathode for an anode-supported proton-conducting solid-oxide fuel cell. *J. Power Sources* **180**, 15-22, (2008).

15 Zeng, Q. *et al.* A Zn-Doped $Ba_{0.5}Sr_{0.5}Co_{0.8}Fe_{0.2}O_{3-\delta}$ Perovskite Cathode with Enhanced ORR Catalytic Activity for SOFCs. *Catalysts* **10**, (2020).

16 Yang, T. *et al.* Evaluation of the CO_2 tolerant cathode for solid oxide fuel cells: Praseodymium oxysulfates/$Ba_{0.5}Sr_{0.5}Co_{0.8}Fe_{0.2}O_{3-\delta}$. *Appl. Surf. Sci.* **472**, 10-15, (2019).

17 Zhang, Y. *et al.* Evaluation of the CO_2 Poisoning Effect on a Highly Active Cathode $SrSc_{0.175}Nb_{0.025}Co_{0.8}O_{3-\delta}$ in the Oxygen Reduction Reaction. *ACS Appl. Mater. Interfaces* **8**, 3003-3011, (2016).

18 Gu, H. *et al.* $SrCo_{0.8}Ti_{0.1}Ta_{0.1}O_{3-\delta}$ perovskite: A new highly active and durable cathode material for intermediate-temperature solid oxide fuel cells. *Composites Part B: Engineering* **213**, 108726, (2021).

19 Li, M. *et al.* A niobium and tantalum co-doped perovskite cathode for solid oxide fuel cells operating below 500 °C. *Nat. Commun.* **8**, 13990, (2017).

20 Gu, B. *et al.* A high performance composite cathode with enhanced CO_2 resistance for low and intermediate-temperature solid oxide fuel cells. *J. Power Sources* **405**, 124-131, (2018).

21 Li, J. *et al.* Enabled fast cathode kinetics for intermediate-temperature solid oxide fuel cell with improved CO_2 poisoning robustness: La_2NiO_4 surfaced-modified $SrCo_{0.8}Nb_{0.1}Ta_{0.1}O_{3-\delta}$ composite. *J. Power Sources* **506**, 230057, (2021).

22 Ding, X. *et al.* Cation deficiency enabled fast oxygen reduction reaction for a novel SOFC cathode with promoted CO_2 tolerance. *Appl. Catal., B* **243**, 546-555, (2019).

23 Lenser, C. *et al.* Performance analysis of a planar solid oxide fuel cell stack between 750 °C and 500 °C. *J. Power Sources* **474**, 228671, (2020).

24 Zhu, Y. *et al.* Promotion of Oxygen Reduction by Exsolved Silver Nanoparticles on a Perovskite Scaffold for Low-Temperature Solid Oxide Fuel Cells. *Nano Lett.* **16**, 512-518, (2016).

25 Zhou, W. *et al.* Novel B-site ordered double perovskite $Ba_2Bi_{0.1}Sc_{0.2}Co_{1.7}O_{6-x}$ for highly efficient oxygen reduction reaction. *Energy Environ. Sci.* **4**, 872-875, (2011).

26 Kiryukhin, V. *et al.* Uncorrelated and correlated nanoscale lattice distortions in the paramagnetic phase of magnetoresistive manganites. *Physical Review B* **70**, 214424, (2004).

27 Xu, X. *et al.* Sc and Ta-doped $SrCoO_{3-\delta}$ perovskite as a high-performance cathode for solid oxide fuel cells. *Composites Part B: Engineering* **178**, 107491, (2019).

28 Zhou, W. *et al.* A Highly Active Perovskite Electrode for the Oxygen Reduction Reaction Below 600 °C. *Angew. Chem. Int. Ed.* **52**, 14036-14040, (2013).

29 Chen, Y. *et al.* A robust fuel cell operated on nearly dry methane at 500 °C enabled by synergistic thermal catalysis and electrocatalysis. *Nat. Energy* **3**, 1042-1050, (2018).

30 Lu, F. *et al.* Heterostructured simple perovskite nanorod-decorated double perovskite cathode for solid oxide fuel cells: Highly catalytic activity, stability and CO_2-durability for oxygen reduction reaction. *Appl. Catal., B* **249**, 19-31, (2019).

31 He, W. *et al.* $BaCo_{0.7}Fe_{0.22}Y_{0.08}O_{3-\delta}$ as an Active Oxygen Reduction Electrocatalyst for Low-Temperature Solid Oxide Fuel Cells below 600 °C. *ACS Energy Lett.* **2**, 301-305, (2017).

32 Yang, G., Shen, J., Chen, Y., Tadé, M. O. & Shao, Z. Cobalt-free $Ba_{0.5}Sr_{0.5}Fe_{0.8}Cu_{0.1}Ti_{0.1}O_{3-\delta}$ as a bi-functional electrode material for solid oxide fuel cells. *J. Power Sources* **298**, 184-192, (2015).

33 Seonyoung Yoo, A. J., Young Wan Ju, Dorj Odkhuu, Junji Hyodo, Hu Young Jeong, Noejung Park, Jeeyoung Shin, Tatsumi Ishihara, Guntae Kim. Development of Double-Perovskite Compounds as Cathode Materials for Low-Temperature Solid Oxide Fuel Cells. *Angew. Chem. Int. Ed.* **126**, 13280-13283, (2014).

34 Chen, Y. *et al.* A Highly Efficient and Robust Nanofiber Cathode for Solid Oxide Fuel Cells. *Adv. Energy Mater.* **7**, 1601890, (2017).

35 Kim, S. *et al.* Nanostructured Double Perovskite Cathode With Low Sintering Temperature For Intermediate Temperature Solid Oxide Fuel Cells. *ChemSusChem* **8**, 3153-3158, (2015).

36 Jun, A. *et al.* Correlation between fast oxygen kinetics and enhanced performance in Fe doped layered perovskite cathodes for solid oxide fuel cells. *J. Mater. Chem. A* **3**, 15082-15090, (2015).

37 Duan, C., Hook, D., Chen, Y., Tong, J. & O'Hayre, R. Zr and Y co-doped perovskite as a stable, high performance cathode for solid oxide fuel cells operating below 500 °C. *Energy Environ. Sci.* **10**, 176-182, (2017).

38 Chen, Y. *et al.* A durable, high-performance hollow-nanofiber cathode for intermediate-temperature fuel cells. *Nano Energy* **26**, 90-99, (2016).

39 Bi, L., Shafi, S. P., Da'as, E. H. & Traversa, E. Tailoring the Cathode–Electrolyte Interface with Nanoparticles for Boosting the Solid Oxide Fuel Cell Performance of Chemically Stable Proton-Conducting Electrolytes. *Small* **14**, 1801231, (2018).

40 Bae, K. *et al.* Demonstrating the potential of yttrium-doped barium zirconate electrolyte for high-performance fuel cells. *Nat. Commun.* **8**, 14553, (2017).

41 Choi, S. M. *et al.* Electrochemical analysis of high-performance protonic ceramic fuel cells based on a columnar-structured thin electrolyte. *Appl. Energ.* **233-234**, 29-36, (2019).

42 An, H. *et al.* A 5×5 cm^2 protonic ceramic fuel cell with a power density of 1.3 W cm^{-2} at 600 °C. *Nat. Energy* **3**, 870-875, (2018).

43 Duan, C. *et al.* Readily processed protonic ceramic fuel cells with high performance at low temperatures. *Science* **349**, 1321-1326, (2015).

44 Choi, S. *et al.* Exceptional power density and stability at intermediate temperatures in protonic ceramic fuel cells. *Nat. Energy* **3**, 202-210, (2018).

45 Lee, J. G., Park, J. H. & Shul, Y. G. Tailoring gadolinium-doped ceria-based solid oxide fuel cells to achieve 2 W cm^{-2} at 550 °C. *Nat. Commun.* **5**, 4045, (2014).

46 Chao, C.-C., Hsu, C.-M., Cui, Y. & Prinz, F. B. Improved Solid Oxide Fuel Cell Performance with Nanostructured Electrolytes. *ACS Nano* **5**, 5692-5696, (2011).